J. Fluid Mech. (1995), *vol.* 291, *pp.* 109–138

Linear and nonlinear baroclinic instability with rigid sidewalls

By MICHAEL D. MUNDT, NICHOLAS H. BRUMMELL AND JOHN E. HART

Department of Astrophysical, Planetary, and Atmospheric Sciences, Campus Box 391, University of Colorado at Boulder, Boulder, CO 80309-0391, USA

(Received 14 December 1993 and in revised form 22 November 1994)

The behaviour of baroclinic waves growing from instability in a two-layer channel flow with rigid (no-slip) sidewalls is described and contrasted with that for the more traditional free-slip boundary conditions. The linear theory for the onset of small-amplitude disturbances shows that the change in lateral boundary conditions has only a modest effect for typical laboratory parameter values, although the no-slip case is slightly more unstable at very small values of bottom friction. On the other hand, the nonlinear evolution of no-slip modes is completely different. While the free-slip case becomes aperiodic only at large values of the supercriticality $(F-F_c)/F_c$, the rigid wall case can be subcritically chaotic. Aperiodic, highly nonlinear wave motions are possible for external control values set in the linearly stable region of parameter space. Weakly nonlinear analysis shows that the no-slip case has a negative Landau constant for moderately small values of bottom friction, and it is in this regime that high-resolution numerical simulations exhibit subcritical chaos. At larger values of bottom friction, the rigid-wall simulations undergo a supercritical quasi-periodic transition to chaos at modest, order one, supercriticality, which is substantially smaller than that required for chaos in the free-slip case.

1. Introduction

Baroclinic instability is recognized as an important process for the generation of waves and eddies in atmospheres and oceans. Such instabilities arise in vertically sheared currents in rotating stably stratified fluids if the effects of friction are sufficiently small and the stratification is relatively weak. Frictional influence is usually measured by a bottom friction parameter Q (defined in §2), which is the ratio of the horizontal advective timescale to the spin down time. Stratification is contained in the rotational Froude number F, which is the square of the ratio of the horizontal lengthscale of the system to the Rossby radius of deformation.

Laboratory experiments on rotating two-layer flow (e.g. Hart 1972, 1985) have shown that the nonlinear evolution of baroclinic waves growing from instability is particularly rich in the Q, F parameter space. Steady equilibration is found when Q is around 1 and the supercriticality $\epsilon = (F-F_c)/F_c$ is not too big (here $F_c(Q)$ is the linear critical point). If Q is held fixed at around 0.2, and the supercriticality is increased from zero, various periodic vacillations of both the wave and zonal-mean fields are observed, followed by chaotic baroclinic motions that can arise at quite small values of $\epsilon \approx 0.4$. Attempts to use weakly nonlinear, low-order, and even fully nonlinear computational models (e.g. Pedlosky 1971; Pedlosky & Frenzen 1980; Hart 1986; Cattaneo & Hart 1990) to explain the laboratory observations have been only moderately successful.

The theories show similar transitions to those observed. However, when important dissipative processes present in the experiments are included (especially frictional effects adjacent to the interface between the two immiscible fluids), then the models fail dramatically to predict the measure of supercriticality needed for chaos. Chaotic behaviour is found only for ϵ exceeding about 5 (for realistic Q) in these models, a factor of 10 or so greater than that observed in the lab.

The models include various assumptions that might be questioned: quasi-geostrophy, linear Ekman layers, channels *vs.* cylindrical geometry, etc. This paper addresses the effects of sidewall boundary conditions on linear and nonlinear baroclinic instability, in the belief that the aforementioned assumptions are less suspect. The previous models all employ stress-free (a.k.a. free-slip) sidewall conditions on the waves, a free-slip constraint on the basic zonal current, and no-slip conditions on secondary corrections to the zonal flow. Such lateral boundary conditions can be formally derived when horizontal momentum diffusion is neglected. Of course, this is not rigorous with respect to the laboratory fluids, where there is at least one vertical sidewall boundary at which a no-slip condition applies to all velocity component. On the other hand, the free-slip situation is computationally simpler. Also, quantitatively successful comparisons of the onset of linear instability based on free-slip eigenfunctions with laboratory experiments encouraged use of this assumption in nonlinear modelling of baroclinic vacillations and chaos.

In this paper we study the dynamics of quasi-geostrophic baroclinic channel flows with no-slip sidewalls. The channel geometry is chosen in order to simplify the complex computations as much as possible. An additional advantage is that this situation can be easily compared with previous theories, and it provides a fundamental reference for future computations in other geometries with perhaps less constraining ageostrophic (modest Rossby number) approximations. The present results show that the horizontal shear of the basic state induced by lateral friction and no-slip has a profound effect on nonlinear equilibration. The presence of the shear relies on no-slip for its existence, but its influence on the equilibration process is largely inviscid in nature. Thus, the results apply to the evolution of finite-amplitude baroclinic waves in the atmosphere, where lateral shears are typically generated by other means but influence the dynamics in an inviscid manner, and in the oceans, where a form of no-slip usually is applied in models, communicated either by lateral eddy diffusion or by bottom friction acting on shoaling topography.

The paper is organized as follows. Section 2 introduces the model geometry and governing equations. The basic state $U(y)$ is derived in §3 and its linear stability properties are calculated in §4. Once the linear eigenfunctions are obtained, it is possible to compute the Landau equation for weakly nonlinear equilibration. This is done in §5 where it is shown that the instability is subcritical for a substantial range of Q. Numerical computations are described in §6. These demonstrate that in the region of subcritical instability, the flow can be chaotic (at negative ϵ!). In §7 more complicated bifurcation structures are educed by employing empirical orthogonal functions, and §8 provides conclusions and suggestions for future work.

2. Governing equations

The model used was originally introduced by Phillips (1954) and has been recently studied by Klein & Pedlosky (1986) and Cattaneo & Hart (1990), among others, in the case with free-slip sidewalls. The system consists of two immiscible fluids, with densities ρ_i and viscosities ν_i, contained in an aspect-ratio 4 rectangular channel, where x is the

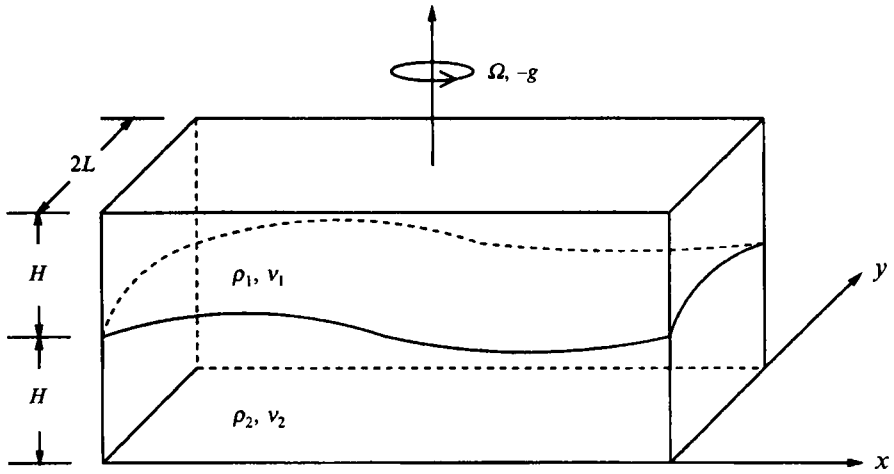

FIGURE 1. Schematic of model geometry.

zonal direction ($0 \leqslant x \leqslant 8$) and y is the meridional direction ($-1 \leqslant y \leqslant 1$). In our case, we consider rigid sidewalls at non-dimensional $y = \pm 1$. We investigate f-plane dynamics in this study, so that the Coriolis parameter $f = 2\Omega$ is constant across the width of the channel. The geometry of the model is shown schematically in figure 1.

Using the quasi-geostrophic approximation, the flow is described by two potential vorticity equations

$$\left[\frac{\partial}{\partial t}+J(P_k,)\right][\nabla^2 P_k+F(-1)^k(P_1-P_2)] = -Q\nabla^2 P_k[(k-1)\chi+(2-k)] + \frac{Q\chi(\nabla^2 P_1-\nabla^2 P_2)(-1)^k}{1+\chi}+\frac{E}{R_o}\nabla^4 P_k, \quad (1)$$

where $k = 1, 2$, $J(f,g) \equiv (\partial f/\partial x)(\partial g/\partial y)-(\partial f/\partial y)(\partial g/\partial x)$, and P_k is the pressure in the kth layer. The second square-bracketed term on the left-hand side of (1) is the potential vorticity of the kth layer. This term is operated on by a time derivative and by a Jacobian. The Jacobian represents advection by the flow in each layer. The first term on the right-hand side of (1) is the Ekman damping at the top and bottom of the channel, while the second term represents interfacial Ekman friction. The last term represents lateral friction, or horizontal diffusion of vorticity. The motions are assumed to be independent of depth within each layer outside the quasi-horizontal Ekman layers. For further discussion and derivation of this model see Pedlosky (1987).

The parameter F is the rotational Froude number,

$$F = \frac{2\Omega^2 L^2(\rho_1+\rho_2)}{gH(\rho_1-\rho_2)}, \quad (2)$$

Q is the bottom friction parameter,

$$Q = L(\nu_1\Omega)^{1/2}/(HU), \quad (3)$$

χ is the viscosity ratio,

$$\chi = (\nu_2/\nu_1)^{1/2}, \quad (4)$$

E is the lateral Ekman number,

$$E = \nu_1/(2\Omega L^2), \quad (5)$$

and R_o is the Rossby number,

$$R_o = U/(2\Omega L). \quad (6)$$

L is the width of the channel, H is the height of each resting layer (which are assumed to be equal), U is a characteristic velocity, LU^{-1} is a characteristic timescale, and g is the gravitational constant. The fluids in the two layers are assumed to have equal viscosities, so that $\chi = 1$. One other constant that does not explicitly appear in the equations is A, the aspect ratio of the channel, which is defined as the ratio of the length of the channel to the width. This parameter determines the physical geometry and is set equal to 4 for this investigation in order to compare to previous studies using free-slip conditions at the sidewalls.

Generally, the parameters which are varied are F and Q. E/R_o, which represents an inverse Reynolds number, is considered fixed at 0.001. Typical values for F and Q are $F_c \approx 1.5 \leqslant F \leqslant 6$ (where F_c is the critical Froude number) and $Q \approx 0.1$. Smaller values of E/R_o are appropriate to some lab experiments. However, computational difficulties arise when E/R_o becomes extremely small or when $Q/(E/R_o)$ becomes too large. The velocities in the two layers are evaluated geostrophically and are given by

$$u_k = -\partial P_k/\partial y, \quad v_k = \partial P_k/\partial x. \tag{7}$$

The height of the interface (from its rest value) is given by

$$h = R_o F(P_2 - P_1). \tag{8}$$

Equation (1) can be re-cast by defining barotropic and baroclinic streamfields according to

$$\Phi_{bt} \equiv \tfrac{1}{2}(P_1 + P_2), \quad \Phi_{bc} \equiv \tfrac{1}{2}(P_1 - P_2). \tag{9}$$

The governing vorticity equations are then

$$\frac{\partial}{\partial t}\nabla^2\Phi_{bt} - J(\nabla^2\Phi_{bt}, \Phi_{bt}) - J(\nabla^2\Phi_{bc}, \Phi_{bc}) = -Q\nabla^2\Phi_{bt} + \frac{E}{R_o}\nabla^4\Phi_{bt}, \tag{10}$$

$$\frac{\partial}{\partial t}[\nabla^2\Phi_{bc} - 2F\Phi_{bc}] - J(\nabla^2\Phi_{bc}, \Phi_{bt}) - J(\nabla^2\Phi_{bt}, \Phi_{bc}) - 2FJ(\Phi_{bt}, \Phi_{bc})$$

$$= -2Q\nabla^2\Phi_{bc} + \frac{E}{R_o}\nabla^4\Phi_{bc}. \tag{11}$$

The barotropic and baroclinic representation is particularly enlightening for this problem, since there is an initial top–bottom symmetry introduced by using equal layer depths and viscosities. The nonlinear evolution of an instability will generally be accompanied by self-generation of a zonal ($v = 0$) current that is superimposed on the basic mean flow $U(y)$. Because of the flip symmetry, a particular wavy instability may generate either a barotropic zonal correction or a baroclinic zonal correction, but not both. These instabilities are termed zonotropic and zonoclinic, respectively. Another important symmetry in the problem is possible invariance under zonal pattern shift by half the basic wavelength followed by reflection about the midline $y = 0$. Cattaneo & Hart (1990) noted that solutions with this shift–reflect symmetry, which corresponds to a 'checkerboard' in wavenumber space, are sometimes preferred by the flow. These solutions are termed 'symmetric', since the velocity at (x, y) is the same as at $(x + \mathscr{L}/2, -y)$, where $\mathscr{L}$ is the channel length. Solutions that do not satisfy this constraint are defined as 'asymmetric'.

For a rigid-wall channel, the boundary conditions are such that

$$\{u_{bt}, u_{bc}\} = 0, \tag{12}$$

$$\{v_{bt}, v_{bc}\} = 0 \tag{13}$$

at $y = \pm 1$. To place a second boundary condition on the zonally averaged portion of the flow (since it trivially satisfies (13)), an appeal is made to mass conservation of the Ekman fluxes originating from the corners where the rigid plates at the top and bottom meet the sidewalls. Because these plates are uniformly translating, there is no interior Ekman suction induced by lid vorticity. However, the Ekman flux at the corners is proportional to the top and bottom wall velocities there, since the geostrophic velocity vanishes as $y \to \pm 1$. These fluxes are assumed to flow down the sidewalls in thin inner boundary layers and to enter the interior uniformly with depth in each layer. This gives rise to an ageostrophic normal velocity $\bar{v}^{(1)}$ next to the wall. Now the zonally averaged momentum equations for the two layers are

$$\frac{\partial \bar{u}_1}{\partial t} + \frac{\partial}{\partial y}(\overline{u_1 v_1}) - \bar{v}_1^{(1)} = \frac{E}{R_o}\frac{\partial^2}{\partial y^2}\bar{u}_1, \tag{14}$$

$$\frac{\partial \bar{u}_2}{\partial t} + \frac{\partial}{\partial y}(\overline{u_2 v_2}) - \bar{v}_2^{(1)} = \frac{E}{R_o}\frac{\partial^2}{\partial y^2}\bar{u}_2, \tag{15}$$

where an overbar denotes a zonal average. Using the fact that the geostrophic velocities equal zero at the sidewalls, and matching the Ekman corner fluxes to the outflows, gives

$$\left.\frac{\partial^2 \bar{u}_{bc}}{\partial y^2}\right|_{y=\pm 1} = -\frac{R_o}{2E}(\bar{v}_1^{(1)} - \bar{v}_2^{(1)}) = -\frac{Q}{2E/R_o}(U_T - U_B) \equiv C_1, \tag{16}$$

$$\left.\frac{\partial^2 \bar{u}_{bt}}{\partial y^2}\right|_{y=\pm 1} = -\frac{R_o}{2E}(\bar{v}_1^{(1)} + \bar{v}_2^{(1)}) = -\frac{Q}{2E/R_o}(U_T + U_B) \equiv C_2, \tag{17}$$

where U_T and U_B are the non-dimensional top and bottom lid velocities, respectively. This zonal flow boundary condition says that the basic-state vorticity gradient at the wall is proportional to U_T and U_B, and vorticity gradients associated with dynamical corrections to the forced zonal flow vanish. Rather than specify U_T and U_B at the beginning, we chose to use a simple basic-state model ((21) below), which in turn determines the necessary wall velocities in a physical realization.

3. Basic state

For a channel with free-slip sidewalls, the simplest flow that satisfies the potential-vorticity equations and boundary conditions is $\bar{u}_{bc} = D_1, \bar{u}_{bt} = D_2$, where the D_j are arbitrary constants. Thus, the basic flow has no dependence on either x or y. For the rigid model, however, the requirement that $u_{bt} = u_{bc} = 0$ at the walls indicates that the velocity must have some meridional dependence on y (unless $u_{bt} = u_{bc} = 0$ everywhere, which is rather uninteresting). An exact solution is obtained from (10), (11). Presuming $\bar{u}_{bt} = 0$, then only (11) survives, and it can subsequently be simplified to yield the exact equation for a parallel zonal basic state:

$$-2Q\frac{\mathrm{d}^2 \Phi_{bc}}{\mathrm{d}y^2} + \frac{E}{R_o}\frac{\mathrm{d}^4 \Phi_{bc}}{\mathrm{d}y^4} = 0. \tag{18}$$

The solution to this is

$$\Phi_{bc} = -y + \frac{\sinh \Gamma y}{\Gamma \cosh \Gamma}, \tag{19}$$

where

$$\Gamma \equiv \left(\frac{2Q}{E/R_o}\right)^{1/2}. \tag{20}$$

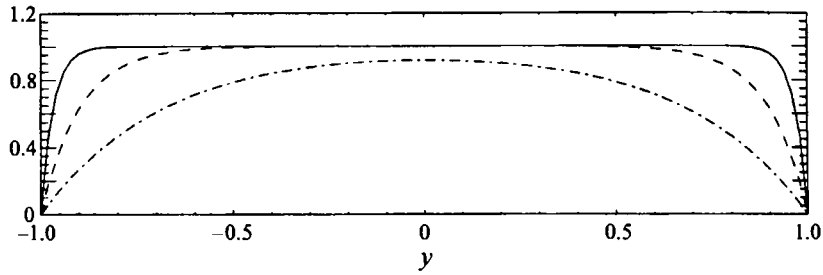

FIGURE 2. Basic-state velocity profiles for $\Gamma = \sqrt{10}$ (dot-dashed line), $\sqrt{100}$ (dashed line), and $\sqrt{1000}$ (solid line).

The boundary-layer thickness is then $O(1/\Gamma) = O(E^{1/4})$, and it is essentially a baroclinic version of the classical Stewartson layer (Stewartson 1957). The resulting baroclinic basic state velocity profile is given by

$$U_{bc} = \frac{-\partial \Phi_{bc}}{\partial y} = 1 - \frac{\cosh \Gamma y}{\cosh \Gamma} \tag{21}$$

(a capital U is used to denote exact basic-state solutions). In terms of boundary conditions on the zonally averaged flow, $C_1 = -\Gamma^2$ and $C_2 = 0$, implying that the upper lid translates uniformly at non-dimensional zonal speed $U_T = 2$, while the lower boundary travels with speed $U_B = -2$. For large Γ, the profile is essentially constant, except near the meridional boundaries where the velocity must approach zero; for $\Gamma \approx O(1)$, the profile resembles more that of a parabola. The velocity profiles are shown in figure 2 for three values of Γ: $\sqrt{10}$, $\sqrt{100}$, and $\sqrt{1000}$.

Plausible values of Γ are physically constrained. In terms of the fundamental parameters,

$$\Gamma^2 = 2\frac{L}{H}\frac{L}{(\nu/\Omega)^{1/2}}. \tag{22}$$

The first term, L/H, is much greater than 1 for geophysical flows and is of $O(1)$ for laboratory experiments. The second term is the ratio of the horizontal lengthscale of the flow to the Ekman layer thickness, a value which is much greater than 1. Thus Γ^2 should be rather large, with values on the order of 100 or so being typical in the laboratory.

4. Linear theory

The linear theory for the onset of instability of the vertically and horizontally sheared basic current with no-slip sidewalls can be approached in the same manner as that for a two-layer model with free-slip sidewalls (Pedlosky 1987), but the details are somewhat more involved. Linearizing (10), (11) about general basic states $U_{bc}(y)$ and $U_{bt}(y)$ yields the following relations:

$$\left[\frac{\partial}{\partial t} + U_{bt}\frac{\partial}{\partial x}\right] q_{bt} + U_{bc}\frac{\partial}{\partial x} q_{bc} + \frac{\partial \phi_{bt}}{\partial x}\frac{\partial \Pi_{bt}}{\partial y} + \frac{\partial \phi_{bc}}{\partial x}\frac{\partial \Pi_{bc}}{\partial y} = -Q\nabla^2 \phi_{bt} + \frac{E}{R_o}\nabla^4 \phi_{bt}, \tag{23}$$

$$\left[\frac{\partial}{\partial t} + U_{bt}\frac{\partial}{\partial x}\right] q_{bc} + U_{bc}\frac{\partial}{\partial x} q_{bt} + \frac{\partial \phi_{bc}}{\partial x}\frac{\partial \Pi_{bt}}{\partial y} + \frac{\partial \phi_{bt}}{\partial x}\frac{\partial \Pi_{bc}}{\partial y} = -2Q\nabla^2 \phi_{bc} + \frac{E}{R_o}\nabla^4 \phi_{bc}. \tag{24}$$

The variables ϕ_{bt} and ϕ_{bc} are the perturbation barotropic and baroclinic stream-

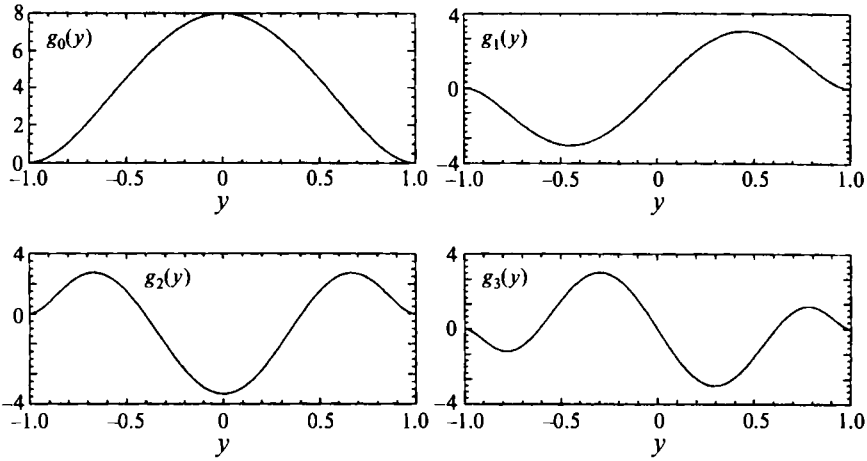

FIGURE 3. First four basis functions $g_i(y)$, $i = 0, 1, 2, 3$, for the rigid, linear instability problem.

functions, while q_{bt} and q_{bc} are, respectively, the barotropic and baroclinic perturbation potential vorticities and are defined as

$$q_{bt} = \nabla^2 \phi_{bt}, \tag{25}$$

$$q_{bc} = \nabla^2 \phi_{bc} - 2F\phi_{bc}. \tag{26}$$

Π_{bt} and Π_{bc} are the potential vorticities of the basic state and have gradients given by

$$\partial \Pi_{bt}/\partial y = -\partial^2 U_{bt}/\partial y^2, \tag{27}$$

$$\partial \Pi_{bc}/\partial y = -\partial^2 U_{bc}/\partial y^2 + 2FU_{bc} = (1 - U_{bc})\Gamma^2 + 2FU_{bc}, \tag{28}$$

and U_{bt} and U_{bc} are, respectively, the barotropic and baroclinic basic-state zonal velocities. U_{bc} is given by (21), while U_{bt} is chosen to be zero for most of the computations presented here. Equation (28) is obtained with the use of (21).

For the slippery-wall model, the governing equations have constant coefficients, since $U_{bc} = 1$. Thus, ϕ_{bt} and ϕ_{bc} can be represented as $e^{ikz}\cos\frac{1}{2}\pi y$, which directly yields $F_c = \frac{1}{2}(k^2 + \frac{1}{4}\pi^2)$ in the inviscid limit. For our rigid-wall model, the no-slip condition on the boundaries suggests that we represent the meridional dependence of ϕ_{bt} and ϕ_{bc} by the family of functions, $g_n(y)$, $n = 0, 1, 2, \ldots$, where

$$g_n(y) = T_{n+4}(y) - \frac{2n+4}{n+1} T_{n+2}(y) + \frac{n+3}{n+1} T_n(y), \tag{29}$$

and

$$T_n(y) = \cos[n \cos^{-1} y] \tag{30}$$

is a Chebyshev polynomial of the first kind. The functions $g_n(y)$ have the property that $g_n(\pm 1) = (\mathrm{d}g_n/\mathrm{d}y)(\pm 1) = 0$ so that the boundary conditions on the velocity are satisfied. Figure 3 displays $g_0(y)$, $g_1(y)$, $g_2(y)$, and $g_3(y)$, showing their rough similarity to trigonometric functions and also revealing narrow layers near the boundaries where $\mathrm{d}g_n/\mathrm{d}y \to 0$.

A disturbance is represented as follows:

$$\phi_{bt} = \mathrm{Re} \sum_{n=0}^{M-1} a_n g_n(y) e^{ik(x-ct)}, \tag{31}$$

$$\phi_{bc} = \mathrm{Re} \sum_{n=0}^{M-1} b_n g_n(y) e^{ik(x-ct)}. \tag{32}$$

The expressions given in (31), (32) are substituted into (23), (24) and the resulting equations are projected back onto the basis functions $g_n(y)$ via a Galerkin procedure. This results in a set of linear, homogeneous equations for the a_n and b_n, yielding an eigenvalue problem for c. The corresponding eigenvector gives the meridional structure of the disturbance. The parameter M is increased to include successively more modes until the results converge. Because of the even symmetry of the basic state about $y = 0$, only those $g_n(y)$ which possess purely even or purely odd symmetry in y are entrained in the initial instability. Thus, in the calculations to follow, we include only the more-unstable even modes as basis functions, so that a resolution of $M = 20$ implies the inclusion of 11 even g_ns.

Γ is the relevant parameter in shaping the basic flow profile. This quantity is kept fixed for stability calculations while the critical value of F is sought for various Q; a choice for Q then automatically determines the value of E/R_o that is to be used. With the barotropic basic state equal to zero, the system has top–bottom antisymmetry. If the system is flipped over and the zonal directions reversed the original system is recovered. The numerical computations confirm that the growing wavy modes are non-propagating ($c_r = 0$, where c_r is the wave phase speed) waves with critical layers at the wall. Figure 4(*a–c*) displays the stability curves for $M = 20$ (i.e. 11 even modes) with Γ equal to $\sqrt{10}$, $\sqrt{100}$, and $\sqrt{1000}$, respectively. The average difference in calculated values of F_c using $M = 18$ instead of $M = 20$ was found to be 0.33%, where the differences were calculated for all curves in figure 4. The largest errors, which are about 3%, occur only when Γ is large and Q is small. Figure 4 show that the rigid model is more stable at large values of Q but less stable at small values of Q. These effects are more pronounced at smaller Γ, and at the extremes of Q for fixed Γ.

What causes the relative destabilization of the rigid-wall flow for small Q? We first observe that the wavy-perturbation boundary layer, which brings tangential velocities to zero at the walls, is typically much thinner than the zonal-flow boundary layer, which has a thickness of $1/\Gamma$. This inner viscous boundary layer for the wave sees $U_{bc} \approx 0$. Additionally, because of the system's inherent symmetries, the numerical results generate meridional dependences of ϕ_{bt} and ϕ_{bc} such that one is purely real and the other is purely imaginary, which allows us to denote the barotropic meridional function as $f(y)$ and the baroclinic function as $g(y)$, where f and g are either purely real or purely imaginary functions. For $y \approx \pm 1$, (23), (24) simplify to yield approximate boundary-layer equations valid near the walls:

$$ik\Gamma^2 g(y) = \frac{E}{R_o}\frac{d^4 f(y)}{dy^4}, \tag{33}$$

$$ik\Gamma^2 f(y) = \frac{E}{R_o}\frac{d^4 g(y)}{dy^4}. \tag{34}$$

In the inner viscous layer, the meridional advection of basic-state vorticity is balanced by the diffusion of perturbation vorticity due to lateral friction. The wave boundary layer thus has a thickness

$$\lambda \equiv (E/R_o/\Gamma^2)^{1/4} = (2Q)^{1/4}/\Gamma \tag{35}$$

given that the zonal wavenumber k is approximately 1. Therefore, the ratio of the wave boundary-layer thickness to the zonal boundary-layer thickness is $(2Q)^{1/4}$, so that the wave viscous boundary layer will be well inside the basic-state shear zone for $Q \ll 1$. This means that the wave essentially sees the basic-state Stewartson layers as inviscid horizontally sheared currents.

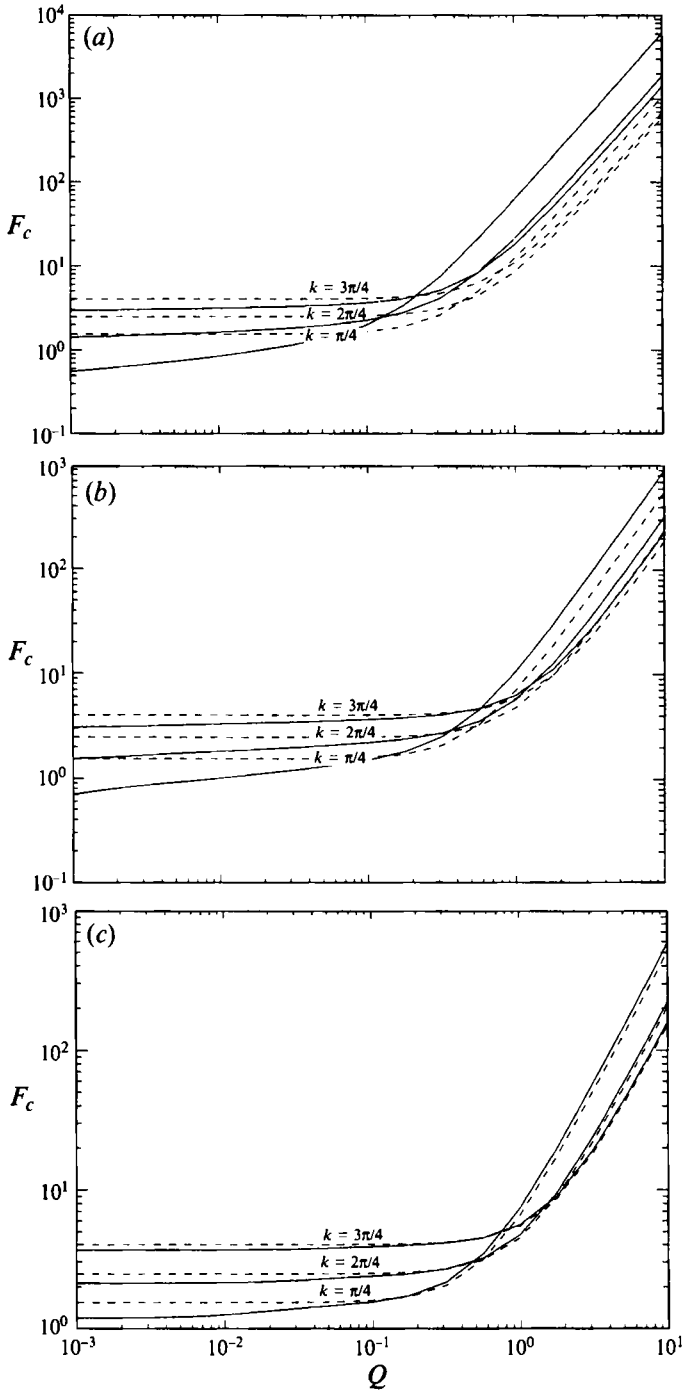

FIGURE 4. Linear stability curves for slippery (dashed line) and rigid (solid line) models: (*a*) $\Gamma = \sqrt{10}$; (*b*) $\Gamma = \sqrt{100}$; (*c*) $\Gamma = \sqrt{1000}$.

Using the above arguments, if the dissipation parameters $(Q, E/R_o)$ are small, the functions $f(y)$ and $g(y)$ outside the wave boundary layer should be similar to those obtained by examining the inviscid form of (23), (24), where terms involving Q and E/R_o are neglected. An exact neutral solution of these inviscid equations which satisfies no normal flow through the walls at $y = \pm 1$ (i.e. no suction out of the inner sidewall layers) is

$$f(y) = U_{bc}(y), \tag{36}$$

$$g(y) = 0, \tag{37}$$

a result previously found by Pedlosky & Klein (1991) in a related problem with no-slip sidewall conditions on the basic state but free-slip on the wavy perturbations. These forms satisfy the inviscid equations only if $F = k^2/2$. The dissipative terms give rise only to a passive boundary layer of thickness λ (given by (35)) so that the no-slip boundary conditions at $y = \pm 1$ are satisfied. A weak boundary suction velocity will occur to modify slightly the boundary conditions on the interior solution shown in (36), (37). A scale analysis reveals that the solution shown in (36), (37) is consistent in generating relatively small dissipative terms when

$$Q \ll 1/\Gamma^4, \tag{38}$$

where (35) is used as an estimate of the boundary-layer thickness for $f(y)$. For values of Q that do not satisfy (38), there will be departures from the behaviour of (36), (37), and the slippery solution itself is a candidate when $1/\Gamma^4 \leqslant Q \ll 1$. In this case Q is small enough so that dissipative terms can be neglected, and Γ is large enough that the flow appears largely uniform in the meridional direction.

Establishing these two solutions as different limits of the nearly inviscid case helps to provide an explanation of the lower stability threshold of the rigid case compared to the free-slip situation. In both limits, the absence of viscosity, coupled with the stipulation that $U_{bt} = 0$, leads to the result that $\phi_{bc} = q_{bc} = 0$ at $F = F_c$. Therefore, at $F = F_c$ (23) vanishes, and (24) reduces to

$$U_{bc}\frac{\partial}{\partial x}q_{bt} + \frac{\partial \phi_{bt}}{\partial x}\frac{\partial \Pi_{bc}}{\partial y} = 0. \tag{39}$$

Thus, at the onset of instability, the zonal advection of the relative vorticity of the barotropic wavy perturbation by the basic-state zonal flow balances the meridional advection of the basic-state potential vorticity by the meridional velocity of the barotropic perturbation. In the slippery case, the basic-state potential vorticity gradient reduces to $2F$, while in the rigid case, there is a non-zero curvature to U_{bc} which gives the basic state the relative vorticity gradient shown in (28). In the limit $Q \ll \Gamma^{-4}$, the meridional advection of the relative vorticity of the basic state by the perturbation meridional flow completely cancels the zonal advection of the $\partial u/\partial y$ portion of the perturbation relative vorticity by the basic flow (more specifically, it is the portion of the perturbation relative vorticity that gives rise to the $\frac{1}{4}\pi^2$ term in the free-slip case), thus yielding $F_c = \frac{1}{2}k^2$. In between the limits where the two solutions are rigorously applicable, these two advective terms partially cancel so that $\frac{1}{2}k^2 < F_c < \frac{1}{2}(k^2 + \frac{1}{4}\pi^2)$.

The above scaling arguments are reflected in the linear numerical calculations. The eigenfunctions were calculated for $Q = 10^{-4}$ and $\Gamma = \sqrt{10}$, where the corresponding value of F_c is 0.43, slightly larger than the theoretical limit of $F_c = \frac{1}{2}k^2 = 0.31$ for $k = \frac{1}{4}\pi$. The barotropic meridional mode (normalized so that its maximum amplitude

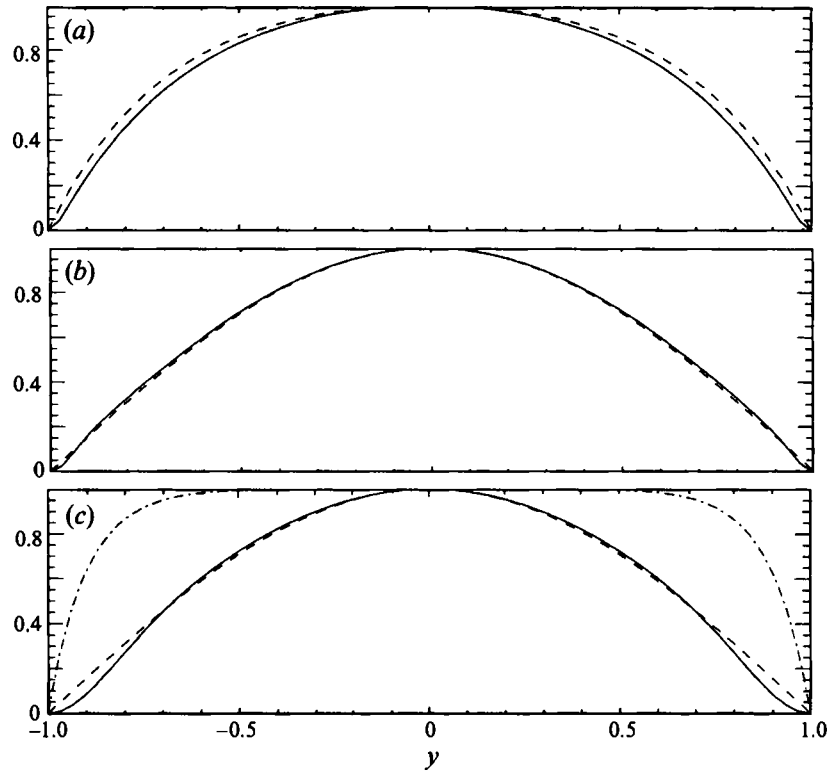

FIGURE 5. Comparison of barotropic eigenfunction (solid line) with: (*a*) basic-state velocity profile $Q = 10^{-4}$, $\Gamma = \sqrt{10}$ (dashed line); (*b*) slippery-case eigenfunction (i.e. $\cos(\pi y/2)$), $Q = 10^{-1}$, $\Gamma = \sqrt{1000}$ (dashed line); (*c*) slippery-case eigenfunction (i.e. $\cos(\pi y/2)$) (dashed line) and basic-state velocity profile, $Q = 10^{-1}$, $\Gamma = \sqrt{100}$ (dot-dashed line). All profiles are normalized to a maximum value of 1 for comparison.

is 1) is shown in figure 5(*a*) along with the basic-state velocity profile. Except for the requisite boundary layers on the barotropic mode at $y = \pm 1$, there is very close agreement between the two shapes. In addition, the scale analysis that yields (38) also predicts that the baroclinic amplitude (relative to the $O(1)$ barotropic amplitude) should be $O(Q^{1/2}\Gamma^2)$ when $Q \ll \Gamma^{-4}$. The numerical results yield an amplitude ratio of 0.14, which is in agreement with the prediction of an amplitude ratio of 0.1 for the parameters used above.

Eigenfunctions were also calculated for $Q = 10^{-1}$ and $\Gamma = \sqrt{1000}$. For this case, $F_c = 1.56$, while the slippery value is $F_c = 1.59$. The rigid-case barotropic eigenfunction and the slippery-case profile, $\cos(\frac{1}{2}\pi y)$, are shown in figure 5(*b*). For comparison, the rigid-case profile is again normalized so that its maximum value is 1. Except for the boundary layers near $y = \pm 1$ for the rigid solution, there is almost exact agreement in the shapes of the profiles. Additionally, the linearized equations predict a baroclinic eigenfunction amplitude of $O(Q) = O(10^{-1})$, while the numerical results yield a value of 0.19, so that the baroclinic eigenfunction is again consistent with the asymptotic analytical predictions. For comparison, the barotropic eigenfunction obtained for $Q = 10^{-1}$ and $\Gamma = \sqrt{100}$ is shown in figure 5(*c*), along with the cosine and basic-state profiles. At this parameter setting, which lies in between the two extremes discussed above, the barotropic eigenfunction is very similar to that obtained for the slippery case (i.e. a cosine solution), although F_c is less than that for free-slip sidewalls.

In summary, the above results indicate that there are two different solutions for small Q, depending on the relative sizes of Q and Γ. For $\Gamma^{-4} \ll Q \ll 1$, the solution approaches that of the slippery case and $F_c = \frac{1}{2}(k^2 + \frac{1}{4}\pi^2)$. For $Q \ll \Gamma^{-4}$ and $Q \ll 1$, the solution approaches that given by Pedlosky & Klein (1991), where the barotropic wavy streamfunction is equal to U_{bc}, the baroclinic streamfunction is zero, and $F_c = \frac{1}{2}k^2$.

In the intermediate region where $\Gamma^{-4} < Q \ll 1$ but $Q\Gamma^4$ is relatively small, the slippery solution is not a good approximation to the rigid-case result. The decrease of F_c with decreasing Γ can be explained by appealing to the energy equation for the perturbations, which is given in Pedlosky (1987) and can be recast in terms of barotropic and baroclinic quantities to yield

$$\begin{aligned}\frac{\mathrm{d}E'}{\mathrm{d}t} = \frac{\mathrm{d}K'}{\mathrm{d}t} + \frac{\mathrm{d}P'}{\mathrm{d}t} = &\int_{-1}^{1} \frac{\partial U_{bc}}{\partial y}\left[\overline{\frac{\partial \phi_{bt}}{\partial x}\frac{\partial \phi_{bc}}{\partial y}} + \overline{\frac{\partial \phi_{bc}}{\partial x}\frac{\partial \phi_{bt}}{\partial y}}\right]\mathrm{d}y \\ &+ \int_{-1}^{1} \frac{\partial U_{bt}}{\partial y}\left[\overline{\frac{\partial \phi_{bt}}{\partial x}\frac{\partial \phi_{bt}}{\partial y}} + \overline{\frac{\partial \phi_{bc}}{\partial x}\frac{\partial \phi_{bc}}{\partial y}}\right]\mathrm{d}y - 2F\int_{-1}^{1} U_{bc}\left[\overline{\phi_{bt}\frac{\partial \phi_{bc}}{\partial x}}\right]\mathrm{d}y \\ &- Q\int_{-1}^{1}\left(\overline{\frac{\partial \phi_{bt}}{\partial x}}\right)^2 + \left(\overline{\frac{\partial \phi_{bt}}{\partial y}}\right)^2 \mathrm{d}y - 2Q\int_{-1}^{1}\left(\overline{\frac{\partial \phi_{bc}}{\partial x}}\right)^2 + \left(\overline{\frac{\partial \phi_{bc}}{\partial y}}\right)^2 \mathrm{d}y \\ &- \frac{E}{R_o}\int_{-1}^{1}\left(\overline{\frac{\partial^2 \phi_{bt}}{\partial x^2}}\right)^2 + 2\left(\overline{\frac{\partial^2 \phi_{bt}}{\partial x\,\partial y}}\right)^2 + \left(\overline{\frac{\partial^2 \phi_{bt}}{\partial y^2}}\right)^2 \mathrm{d}y \\ &- \frac{E}{R_o}\int_{-1}^{1}\left(\overline{\frac{\partial^2 \phi_{bc}}{\partial x^2}}\right)^2 + 2\left(\overline{\frac{\partial^2 \phi_{bc}}{\partial x\,\partial y}}\right)^2 + \left(\overline{\frac{\partial^2 \phi_{bc}}{\partial y^2}}\right)^2 \mathrm{d}y. \end{aligned} \tag{40}$$

The left-hand side of the equation is the time rate of change of perturbation energy, partitioned into the perturbation kinetic energy (K') and the perturbation potential energy (P'). The right-hand side comprises several terms. The first two are the barotropic energy transfer terms. These depend on the meridional structure of the basic state. For our present purposes, U_{bt} is zero and the second term thus vanishes. The first term represents the conversion of the basic-state kinetic energy directly into perturbation energy. The third term is the baroclinic transfer term, which converts available potential energy of the basic state into perturbation energy and depends only on the vertical structure of the basic state. The fourth and fifth terms denote the energy loss due to bottom friction; similarly, the last two terms represent the dissipation from lateral friction.

The linear numerical results show that as the horizontal shear layer of the mean flow widens (i.e. Γ decreases), there is a marked increase in the magnitude of the barotropic energy transfer term. However, this term is negative for all the cases considered here, which indicates that the barotropic transfer term is taking energy from the perturbations and placing it back in the basic U_{bc} profile. The barotropic energy transfer is thus not responsible for the lowering of F_c with decreasing Γ and in fact produces a stabilizing effect. However, the frictional terms in (40) become smaller as Γ decreases and in fact more than offset the barotropic transfer, resulting in a decrease of F_c.

Finally, the behaviour of the flow at large Q merits a brief discussion. Referring to figure 4, the large-Q solutions obtained for smaller Γ indicate that the no-slip flow is noticeably more stable than the free-slip case, while solutions for larger Γ approach the slippery results. This phenomenon can be understood by again appealing to the energy transfers occurring within the system. The barotropic transfer is essentially zero for all values of Γ considered. Thus, at $F = F_c$ there is a balance between baroclinic energy

conversion and dissipation. As Γ increases, the magnitude of the lateral dissipation decreases with respect to that of the bottom friction (which is not unexpected, since E/R_o is decreasing), and the overall magnitudes of both types of dissipation decrease, thus lowering F_c and moving it towards the free-slip value. For smaller Γ the free-slip solution is not a good approximation owing to the large horizontal shear layers in the basic flow, and this results in an increase in F_c from the free-slip value.

The results presented above indicate a substantial difference in the stability curves for the rigid-wall and free-slip cases at extreme (small or large) values of Q. For $Q \approx 0.1$–1.0, however, the differences can be insignificant. Hart (1972) found that the stability curves of a free-slip model agreed well with those obtained from laboratory experiments in a cylinder (which necessarily has a single rigid wall). These laboratory results were obtained in the range $O(10^{-1}) < Q < O(1)$ and with $\Gamma \approx \sqrt{200}$. As is evident from figure 4(*b*), this is indeed the region where the two solutions closely coincide, so that the agreement found between experiment and free-slip theory would appear to be an artifact of being in a regime where stabilization due to rigid no-slip boundary conditions on the waves, and destabilization due to the presence of a y-dependent basic state, roughly balance.

Another twist is that in the laboratory the upper layer is usually driven from above by a differentially rotating lid. This gives the upper layer a non-dimensional velocity of 3, while the lower layer has a non-dimensional velocity of 1 (Hart 1972). For the channel analogue this yields $U_{bt} = 2$, $U_{bc} = 1$ in the interior of the flow. The stability problem differs fundamentally from that previously discussed because a barotropic basic state allows critical layers in the flow's interior. In other words, the vertical asymmetry of the problem causes the wavy perturbations to have a phase speed which is approximately equal to U_{bt}. Therefore, since the velocity must approach zero near the walls, in the upper layer only there will be a value of y for which the upper-layer velocity $U_1 = c_r$, where c_r is the phase speed of the wavy perturbation. At the onset of instability, $c_i = 0$, so that the inviscid form of the equations contains a singularity. Although the presence of dissipation avoids a singular set of equations, one might anticipate significant changes in the eigenfunctions near the critical layer for small to moderate values of Q.

To investigate this problem, a barotropic basic state of the form

$$\Phi_{bt} = 2\left[-y + \frac{\sinh \hat{\Gamma} y}{\hat{\Gamma} \cosh \hat{\Gamma}}\right] \tag{41}$$

is added, where

$$\hat{\Gamma} \equiv \left(\frac{Q}{E/R_o}\right)^{1/2} = \Gamma/\sqrt{2}. \tag{42}$$

Note that (41) is the exact solution to (10). The barotropic basic-state velocity profile is then

$$U_{bt} = \frac{-\partial \Phi_{bt}}{\partial y} = 2\left[1 - \frac{\cosh \hat{\Gamma} y}{\cosh \hat{\Gamma}}\right]. \tag{43}$$

Linear stability curves for $0.01 \leqslant Q \leqslant 10$ and $\Gamma = \sqrt{10}$, $\sqrt{100}$, and $\sqrt{1000}$ are shown in figure 6(*a*–*c*). A value of $M = 20$ cross-stream modes (again including only the even eigenfunctions) was used for all calculations. Stability curves were also found using $M = 18$ and $M = 24$, and noticeable differences were found only for $Q \approx 0.01$.

For $\Gamma = \sqrt{10}$, there are substantial differences in the stability curves between the two rigid-wall cases. The case with $U_{bt} \neq 0$ is generally more stable for $Q \geqslant 1$. For small

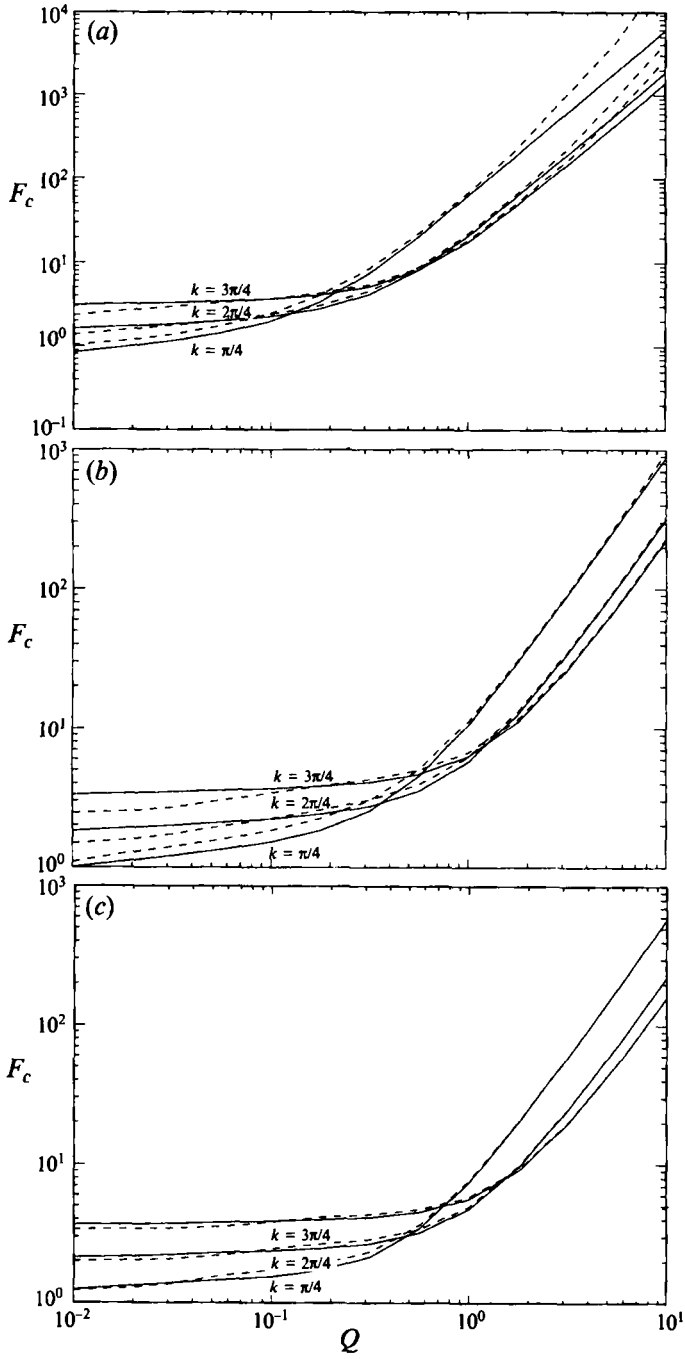

FIGURE 6. Linear stability curves for rigid model with $U_{bt} = 0$ (solid line) and $U_{bt} \neq 0$ (dashed line); (*a*) $\Gamma = \sqrt{10}$, (*b*) $\Gamma = \sqrt{100}$, (*c*) $\Gamma = \sqrt{1000}$.

values of Q, however, the $k = 2\pi/4$ and $3\pi/4$ waves are less stable than their $U_{bt} = 0$ counterparts. For $\Gamma = \sqrt{100}$, shown in figure 6(*b*), the situation is similar. However, for large Q, the two cases agree much better. Finally, for $\Gamma = \sqrt{1000}$, where the zonal shear layers are trapped in a thin viscous region near the wall, the curves agree almost exactly for large Q. For intermediate values of Q, the situation with $U_{bt} \neq 0$ is more

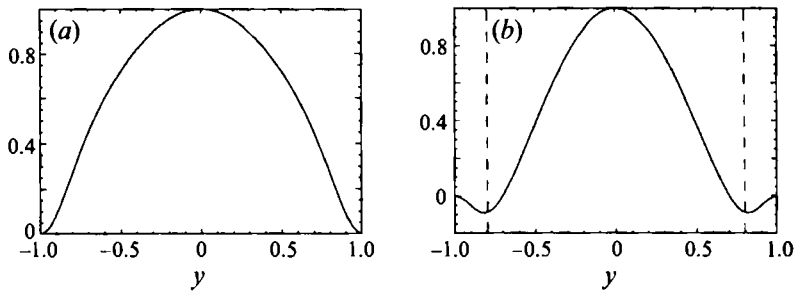

FIGURE 7. Imaginary parts of eigenfunctions of barotropic perturbations with (*a*) $U_{bt} = 0$ and (*b*) $U_{bt} \neq 0$, for $\Gamma = \sqrt{100}$, $Q = 0.1$, $k = \frac{1}{2}\pi$. The dashed lines show the critical layer where $U_{bt} = c_r$.

stable for all k, and for small Q, F_c values are slightly lower when $U_{bt} \neq 0$. Nonetheless, the differences in critical values are again small for Q values typical of laboratory experiments.

Figure 7 shows the imaginary part of the barotropic eigenfunction for both situations for $\Gamma = \sqrt{100}$, $Q = 0.1$, and $k = \frac{1}{4}\pi$. In the figure, the eigenfunctions have both been normalized to 1, and the critical layer (i.e. the value of y for which $U_{bt} = c_r$) for the second case is shown by the dashed vertical lines. When $U_{bt} \neq 0$, the eigenfunction undergoes substantial variation as it passes through the critical layer. This does not occur when $U_{bt} = 0$. A similar variation in the eigenfunction when y is at or near the critical layer is observed for all values of Γ.

5. Weakly nonlinear theory

A normal-mode cascade model was constructed to examine the finite-amplitude fate of the no-slip instabilities discussed in §4. The method follows Pedlosky (1970, 1971, 1972), who examined the evolution of initially small wavy perturbations in a channel with free-slip sidewalls. This expansion procedure yields an amplitude equation with form

$$\mathrm{d}A/\mathrm{d}t = A - \gamma A^3 + \text{h.o.t.}, \tag{44}$$

where A is the amplitude of the wavy perturbation, γ is the Landau constant, and h.o.t. indicates higher-order terms. In Equation 44, the time is scaled by the reciprocal of the linear growth rate. A supercritical bifurcation will have $\gamma > 0$, so that the nonlinear term brings the amplitude to an eventual equilibration. However, a subcritical bifurcation occurs if $\gamma < 0$ so that the lowest nonlinearity of the equation actually destabilizes the steady state, predicting an infinite amplitude in a finite time. It is important to note that (44) is first order. This will occur when the supercriticality parameter

$$\Delta \equiv (F - F_c) \tag{45}$$

is small enough that frictional effects are much larger than inviscid growth (i.e. $Q/\Delta \gg 1$). Since we are concerned here with the dynamics arbitrarily close to the neutral curve, we are free to choose Δ small enough such that frictional effects are important. In the event that $Q \lesssim \Delta^{1/2}$, the dynamics are described by a higher-order system (see Pedlosky 1970, 1971, 1972).

To arrive at (44), we expand the finite-amplitude perturbation in powers of $\Delta^{1/2}$. We write

$$\phi_{bt} = \Delta^{1/2}\phi_{bt}^{(1)} + \Delta\phi_{bt}^{(2)} + \Delta^{3/2}\phi_{bt}^{(3)} + \ldots, \tag{46}$$

$$\phi_{bc} = \Delta^{1/2}\phi_{bc}^{(1)} + \Delta\phi_{bc}^{(2)} + \Delta^{3/2}\phi_{bc}^{(3)} + \ldots, \tag{47}$$

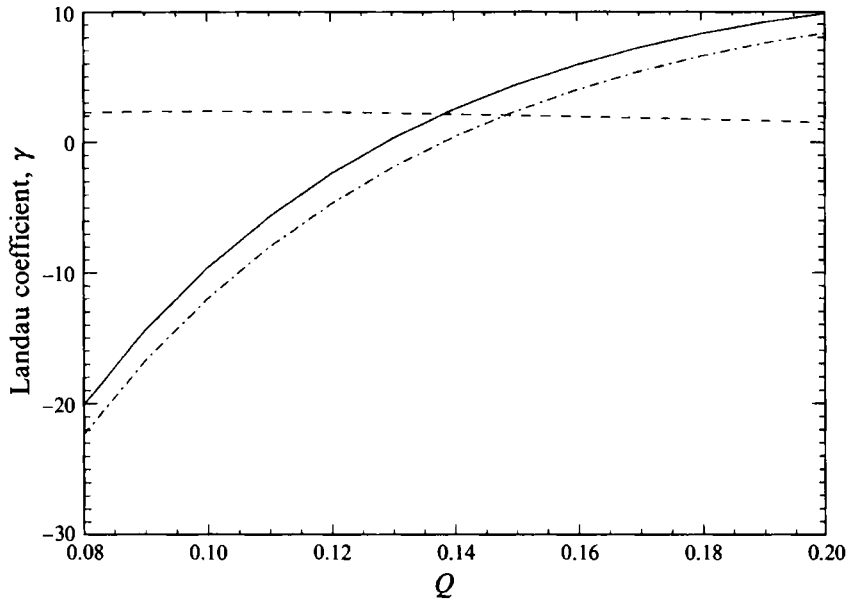

FIGURE 8. Landau coefficient (γ) versus Q. The solid line shows the overall coefficient, while the dashed and dot-dashed lines show the wave–wave and wave–mean contributions, respectively.

where the superscript indicates the order and $\phi_{bt}^{(i)}$ and $\phi_{bc}^{(i)}$ are all $O(1)$ variables. We also stipulate that our new time variable, T, be scaled such that

$$\partial/\partial t = \Delta\partial/\partial T. \tag{48}$$

Finally, we specify that ϕ_{bt} and ϕ_{bc} have a slow time dependence given by $A(T)$.

Isolating all terms of $O(\Delta^{1/2})$, we obtain

$$\mathsf{L}[\phi_{bt}^{(1)}\ \phi_{bc}^{(1)}]^T = 0. \tag{49}$$

Here, L is a linear differential operator matrix whose elements are given by (23), (24). Solving this set of equations with no-slip boundary conditions yields F_c and the linear eigenfunctions. At $O(\Delta)$, we find

$$\mathsf{L}[\phi_{bt}^{(2)}\ \phi_{bc}^{(2)}]^T = [R_1^{(2)}\ R_2^{(2)}]^T. \tag{50}$$

The right-hand side consists of the nonlinear interactions of the $O(\Delta^{1/2})$ solution. From this equation, we obtain two particular solutions – one that is proportional to e^{2ikx} and one that is a function of y only. These are the second zonal harmonic and the mean-flow correction generated directly by the nonlinear interactions of the linear eigenfunctions. Finally, at $O(\Delta^{3/2})$, we obtain

$$\mathsf{L}[\phi_{bt}^{(3)}\ \phi_{bc}^{(3)}]^T = [R_1^{(3)}\ R_2^{(3)}]^T. \tag{51}$$

In this case the right-hand side contains terms that resonate with the left-hand side. In order that the solution be valid, these terms must not project onto the eigenfunctions of the adjoint linear problem, which are proportional to e^{ikx}. This creates a solvability condition that yields the Landau equation, allowing us to determine γ. The actual calculations are quite tedious, and progress was only possible by using a symbolic manipulator. The linear eigenfunctions $\phi_{bt}^{(1)}, \phi_{bc}^{(1)}$ each contain seven even terms of the Chebyshev expansion shown in (31), (32) (the differences obtained using five terms are insignificant).

The results are shown in figure 8. These were calculated with $E/R_o = 0.001$, so that

an increase in Q implies a corresponding increase in Γ. The Landau coefficient is negative for $Q < 0.13$, rendering the instability subcritical. In addition, it is the wave–mean flow interaction that yields a negative γ. The wave–wave interactions are stabilizing for all Q. Because the wavy eigenfunctions are similar to those in the free-slip case, one might have expected the wave–mean interactions to still be stabilizing; however, the alteration of the basic-state flow in going from free-slip to no-slip conditions completely changes the character of the wave–mean interactions.

To identify the physical mechanism responsible for the negative Landau coefficient, the nonlinear terms that combine to yield the wave–mean portion of the Landau coefficient (i.e. the destabilising part) were compared with their counterparts in the slippery case, in which the wave–mean portion of the Landau coefficient is positive and thus stabilizing. Figure 9(*a*) displays the contributions from the various nonlinear terms for the slippery case, while those for the rigid solution are displayed in figure 9(*b*). The J_i terms are defined as follows:

$$J_1 = \int_{-1}^{1} \tilde{\phi}_{bt}^{(1)} \left(-\bar{u}_{bc}^{(2)} \frac{\partial}{\partial x} \omega_{bc}^{\prime(1)} \right) \mathrm{d}y, \tag{52}$$

$$J_2 = \int_{-1}^{1} \tilde{\phi}_{bt}^{(1)} \left(-v_{bc}^{\prime(1)} \frac{\partial}{\partial y} \bar{\omega}_{bc}^{(2)} \right) \mathrm{d}y, \tag{53}$$

$$J_3 = \int_{-1}^{1} \tilde{\phi}_{bc}^{(1)} \left(-v_{bt}^{\prime(1)} \frac{\partial}{\partial y} \bar{\omega}_{bc}^{(2)} \right) \mathrm{d}y, \tag{54}$$

$$J_4 = \int_{-1}^{1} \tilde{\phi}_{bc}^{(1)} \left(-\bar{u}_{bc}^{(2)} \frac{\partial}{\partial x} \omega_{bt}^{\prime(1)} \right) \mathrm{d}y, \tag{55}$$

$$J_5 = \int_{-1}^{1} \tilde{\phi}_{bc}^{(1)} \left(-v_{bt}^{\prime(1)} 2F \frac{\partial}{\partial y} \bar{\phi}_{bc}^{(2)} \right) \mathrm{d}y, \tag{56}$$

where $\omega_{bc} \equiv \nabla^2 \phi_{bc}$ and $\omega_{bt} \equiv \nabla^2 \phi_{bt}$. J_1 is the zonal advection of wavy baroclinic relative vorticity by the zonal flow, J_2 is the meridional advection of zonal relative vorticity by the baroclinic wavy perturbation, J_3 is the meridional advection of zonal relative vorticity by the barotropic wavy perturbation, J_4 is the zonal advection of wavy barotropic relative vorticity by the zonal flow, and J_5 is the meridional advection of zonal baroclinic vorticity due to interface stretching by the barotropic wavy perturbation. In addition, the tilde indicates the adjoint solutions, the prime indicates wavy quantities, and the overbar indicates zonally averaged variables. In figure 9, the plots are normalized by the total contribution to the Landau coefficient at $Q = 0.08$. Although the respective magnitudes of the J_i are different between the two cases, only J_3 in the rigid case possesses a sign opposite to that of its slippery counterpart. Thus, the barotropic wave field advects zonal vorticity in such a way that it enhances its own growth rate against the background state.

The quantity J_3, which has an $O(1)$ stabilizing effect in the free-slip case, has an $O(1)$ destabilizing contribution in the rigid formulation. In fact, the change of sign of J_3 coincides closely with the change of sign of the entire contribution from the wave–mean interactions to the Landau coefficient. Indeed, if one examines the slippery case for $Q \ll 1$, then J_1 and J_2 can be shown to be $O(Q^2)$ with respect to the remaining J_i. In addition, although J_4 and J_5 are $O(1)$, their difference is also $O(Q^2)$. Therefore, J_3 is left as the only remaining $O(1)$ contribution to the Landau coefficient. Moreover, the difference between J_3 in the slippery and rigid cases can be traced to a single term in J_3, $\partial \bar{\omega}_{bc}^{(2)}/\partial y = \partial^3 \bar{\phi}_{bc}^{(2)}/\partial y^3$, since the product of the other two terms, $v_{bt}' \tilde{\phi}_{bc}$, has almost the

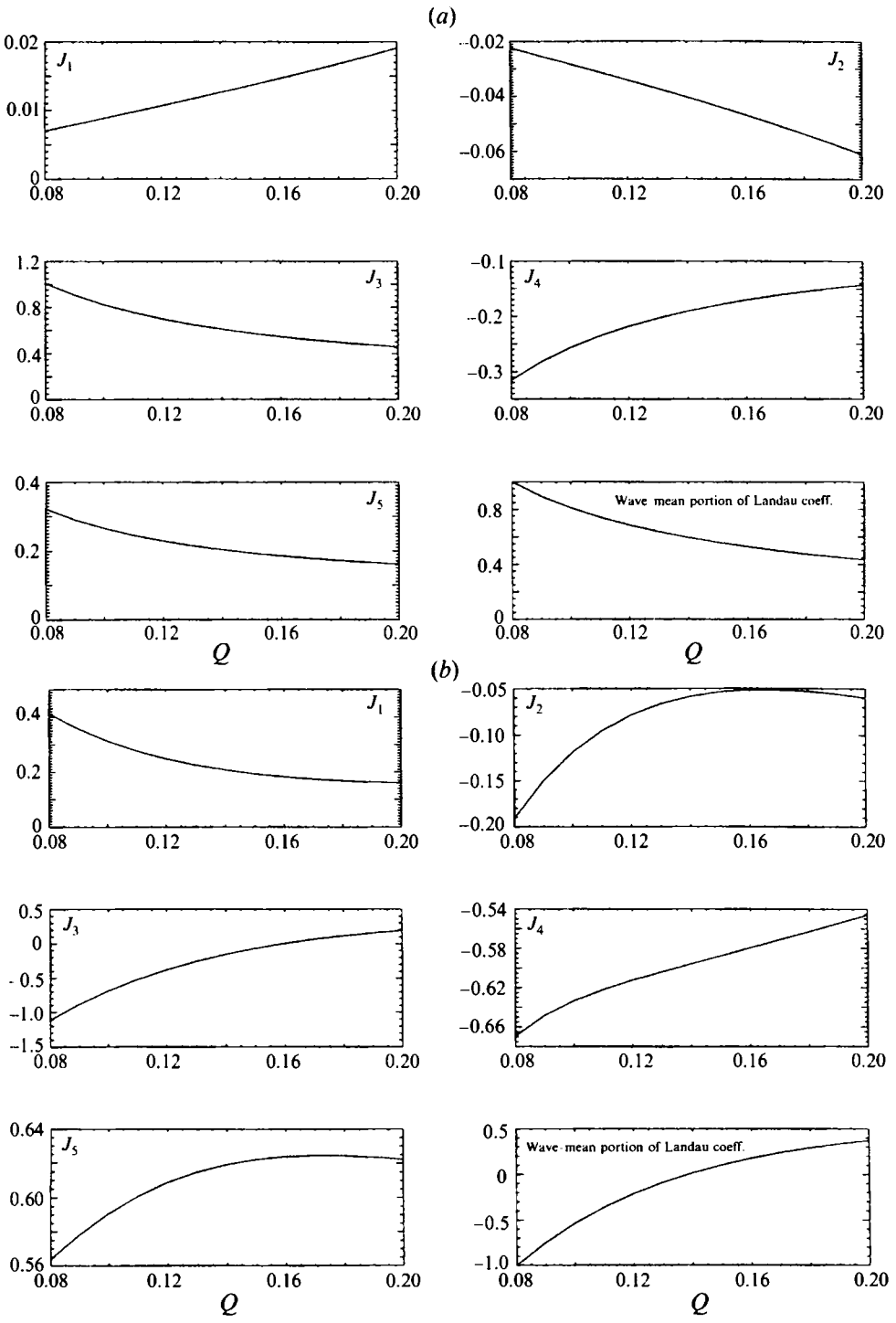

FIGURE 9. Contribution by nonlinear wave-zonal interactions to Landau coefficient, for $E/R_0 = 0.001$: (*a*) slippery case, (*b*) rigid case. The plots have been normalized by the total wave–mean contribution to the Landau coefficient at $Q = 0.08$. The J_i terms are defined in the text.

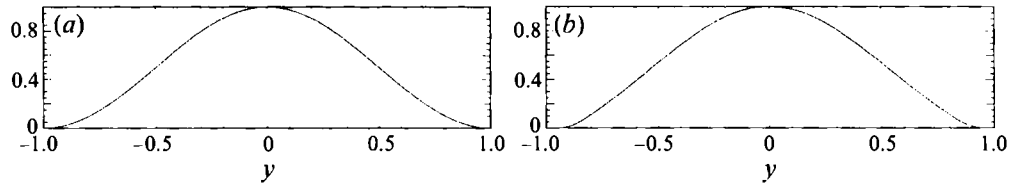

FIGURE 10. $v'_{bt}\tilde{\phi}_{bc}$ versus y for (a) slippery and (b) rigid cases, $Q = 0.08$.

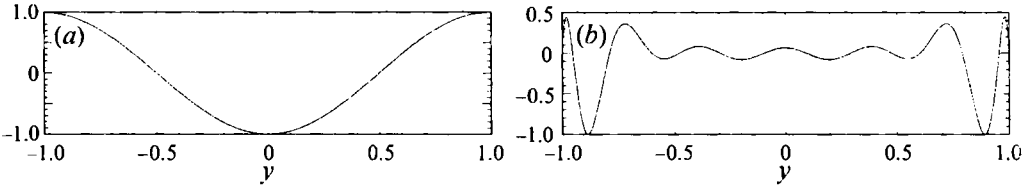

FIGURE 11. Zonal vorticity gradients versus y for (a) slippery and (b) rigid cases, $Q = 0.08$.

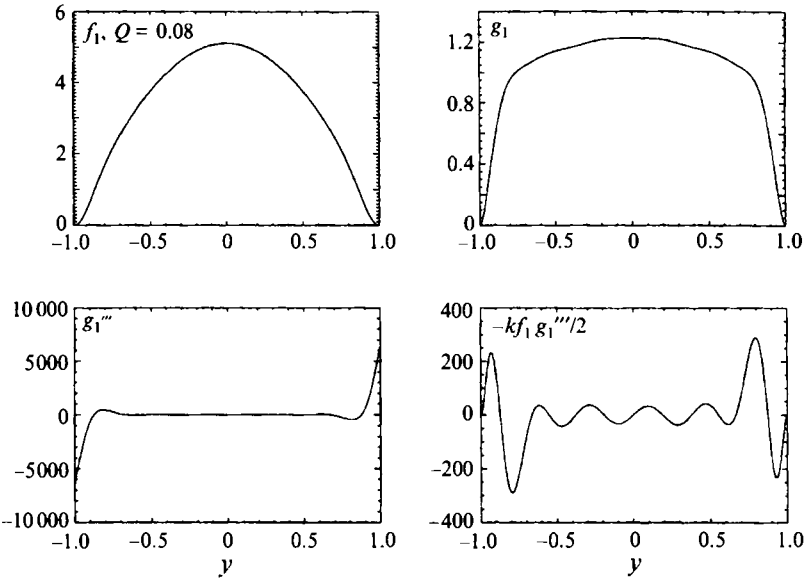

FIGURE 12. Contributions to forcing of zonal-correction equation, rigid case, $Q = 0.08$.

same shape in both the rigid and slippery cases, as figure 10 shows. The free-slip and rigid zonal-correction vorticity gradients are shown (for $Q = 0.08$) in figure 11, and the amplitudes are normalized to 1 for convenience. In the rigid case, the large amplitude deviations near the walls, which correspond to large vorticity gradients, change the sign of J_3 from positive to negative for smaller values of Q. Thus, the subcritical instability owes its existence entirely to the presence of rigid sidewalls via the generation of very different basic-state vorticity gradients. As Q increases and the basic profile approaches that of the free-slip case, J_3 becomes positive and the instability becomes supercritical.

These profound differences in the second-order, zonal-correction gradients can in turn be traced back to the shapes of the linearly unstable wavy eigenfunctions. The equation for the baroclinic zonal correction can be written schematically as

$$2Q\frac{\partial^2\bar{\phi}_{bc}^{(2)}}{\partial y^2} - \frac{E}{R_o}\frac{\partial^4\bar{\phi}_{bc}^{(2)}}{\partial y^4} = \mathscr{R}, \tag{57}$$

where $\bar{\phi}_{bc}^{(2)}$ is the second-order, baroclinic zonal-correction term and $\mathscr{R}$ denotes the right-hand-side forcing. This equation is dominated on the left-hand side by the fourth derivative term, and the right-hand side is a result of the nonlinear interactions of the first-order terms. These nonlinear terms give rise to large derivatives near the walls, thus causing the shape of the zonal correction to deviate significantly from the free-slip case. The right-hand side is dominated by the term $-kf_1 g_1'''/2$, representing the meridional advection of baroclinic vorticity by the barotropic meridional velocity, where f_1 is the barotropic meridional eigenfunction and g_1 is the baroclinic meridional eigenfunction. The functions f_1, g_1, g_1''', and $-kf_1 g_1'''/2$ for $Q = 0.08$ are shown in figure 12. The shape of the nonlinear term is similar to that of the vorticity gradient for the rigid case shown in figure 11 and thus reveals the origin of the zonal correction's shape (in fact, the antiderivative of $-kf_1 g_1'''/2$ is approximately the vorticity gradient). In contrast, the eigenfunctions and nonlinear terms in the slippery case are sine and cosine functions, giving rise to the cosinusoidal zonal vorticity gradient of figure 11 (*a*).

6. Fully nonlinear model

The weakly nonlinear analysis shows that, in comparison to the model with free-slip sidewalls, very different and potentially very interesting dynamics are possible when the supercriticality $(F-F_c)/F_c$ is small or even negative. What happens, for instance, when $\gamma < 0$? To investigate this situation (among others), high-resolution numerical simulations were utilized. We now describe computational solutions of (10) and (11) with $U_{bt} = 0$, so that only a baroclinic basic state exists.

6.1. *Numerical method*

The numerical model implements a pseudo-spectral method, where linear terms are computed in spectral space, while nonlinear terms are computed in physical space. Conversions between the two spaces are carried out by fast transform methods. The time discretization is semi-implicit: the linear terms are updated using an implicit Crank–Nicholson scheme, while the nonlinear terms are marched forward with an explicit three-level Adams–Bashforth method. Owing to the nature of the boundary conditions, the spatial discretization in the two directions is different, utilizing Fourier modes in the zonal direction and Chebyshev polynomials in the meridional. Since the Chebyshev functions do not individually satisfy the rigid boundary conditions (i.e. no-slip and impenetrable), they are combined using a 'tau' method in order to meet the necessary requirements (Canuto *et al.* 1988). Unlike a model with free-slip sidewalls, in the rigid-wall formulation there are no boundary conditions on the vorticity for the wavy portions of the flow. To overcome this problem, a modification of the influence matrix technique (Kleiser & Schumann 1980) is used.

The model was run at two different resolutions: 64×33 and 128×65. The higher-resolution runs were compared to those performed at lower resolution near transition points in parameter space, especially near the onset of chaos. No substantial difference in results was found between the two resolutions. Consequently, a resolution of 64×33 was deemed adequate to provide convergent results (especially since, as opposed to the free-slip case, most of the interesting behaviour occurs for $F \approx F_c$). The code was validated against the linear theory of §4.

6.2. *Results*

Numerical runs were made for variable F with $Q = 0.08, 0.10, 0.125, 0.15$ and 0.20. The critical values of F for the above parameter settings are approximately 1.44, 1.52, 1.60,

1.67 and 1.81, respectively. One run was also made for variable Q with $F = 1.90$. For all of the computations, E/R_0 was kept fixed at 0.001. Solutions for variable F were initially obtained by starting just above F_c and sequentially increasing F to examine any changes in behaviour. For these parameter settings, the free-slip model shows mainly steady, and at most periodic, behaviour.

The results for the no-slip model are shown in figure 13. For $Q = 0.2$, the bifurcation structure is similar to that seen in the computational simulations with free-slip conditions (Cattaneo & Hart 1990; Mundt & Hart 1995), i.e. S → AV → QP → C, with AV indicating periodic amplitude vacillation. However, in the free-slip case this transition to chaos is found only for $Q \leqslant 0.05$ and $F \gtrsim 8$. Over the range of Q and F shown in figure 13(*a*), the free-slip case becomes periodic at $F \gtrsim 4$. In the no-slip case for $0.08 \leqslant Q \leqslant 0.15$, however, the behaviour is not steady, but rather periodic or chaotic. The fact that the amplitude of these motions does not approach 0 at F_c confirms that the instabilities born at F_c are subcritical, as expected from the results of §5. In figure 13(*b*), the solutions are obtained by starting with a solution for $F > F_c$ and using this as an initial state to find a solution for $F < F_c$. The subcritical region is quite large for $Q = 0.08$ but nearly disappears for $Q = 0.15$. Hysteresis occurs in the investigations made for $F = 1.9$ with variable Q; in the region $0.12 < Q < 0.15$, a stable solution exhibiting amplitude vacillation can also be found, though it is unstable to sufficiently large asymmetric perturbations. Although not shown in figure 13, a set of runs was performed for $Q = 0.5$. The results display only steady behaviour until $O(10)$ supercriticality and thus will not be discussed further.

The hysteresis that arises due to the subcritical dynamics yields multiple solutions for a given parameter value. Generally, the solutions differ in their temporal behaviour and spatial structure, a result of breaking the shift–reflect wave symmetry. However, in certain regions where figure 13 indicates AV behaviour, there can exist AV with or without a barotropic zonal correction. In this case, the solutions differ in their top–bottom symmetry, but their temporal behaviour is nearly identical. In figure 13, the AV regimes always exhibit a symmetric, or shift–reflect, wave symmetry; conversely, the QP regions nearly always have an asymmetric wave field, in which all waves may possess non-zero energy.

The behaviour at $Q = 0.1$ is especially interesting because of the subcritical behaviour at $F_c = 1.52$ and also due to the fact that the asymptotic state of the system is chaotic at F_c. Small, random initial conditions quickly settle into a symmetric, AV regime with no barotropic zonal corrections. A time trace of the lowest symmetric baroclinic zonal correction, calculated at $F = 1.53$, is shown in figure 14. Once the flow enters AV, the asymmetric barotropic zonal correction (also shown in figure 14), which was zero during the initial growth of the wavy perturbations, grows to finite amplitude starting at $t \approx 300$. This instability, whose dominant frequency is slightly less than half that of the amplitude vacillation, appears to result in a quasi-periodic solution. However, around $t \approx 800$, the remaining two possible symmetry-breaking instabilities (i.e. the asymmetric zonoclinic and symmetric zonotropic types) start to grow just after the system has seemingly settled into a QP state. These modes both eventually attain the same magnitude as the others, and the system behaves chaotically.

Figure 13(*a*) shows that at $Q = 0.08$ the flow also becomes chaotic. In this situation, there is an initial onset of AV, just as for $Q = 0.10$. Subsequent to this, however, all of the remaining zonal modes, i.e. symmetric barotropic, asymmetric barotropic, and asymmetric baroclinic, grow and reach finite amplitude nearly simultaneously. Thus, in this situation all the symmetries of the problem are broken concurrently. The end result is chaotic behaviour similar to that seen at $Q = 0.10$. Figure 15(*e*) displays a

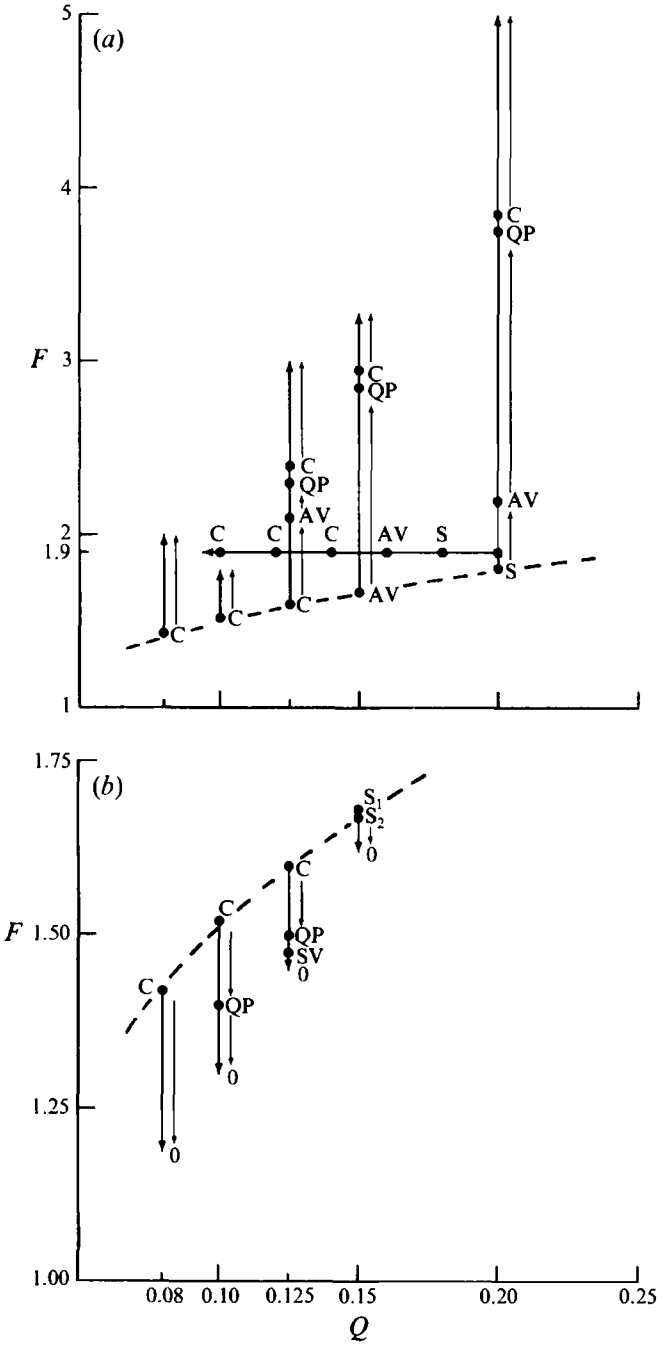

FIGURE 13. Regime diagram for rigid-wall model with (*a*) increasingly supercritical parameters and (*b*) decreasingly supercritical and subcritical parameters. The solutions are obtained by following the arrows in the direction indicated in the (F, Q)-plane. Note that they are in opposite directions in (*a*) and (*b*). 0 denotes the basic-state solution, *S* denotes steady behaviour, AV denotes periodic amplitude vacillation, QP denotes quasi-periodicity, C denotes chaos, and SV denotes periodic structural vacillation. The dashed line indicates F_c.

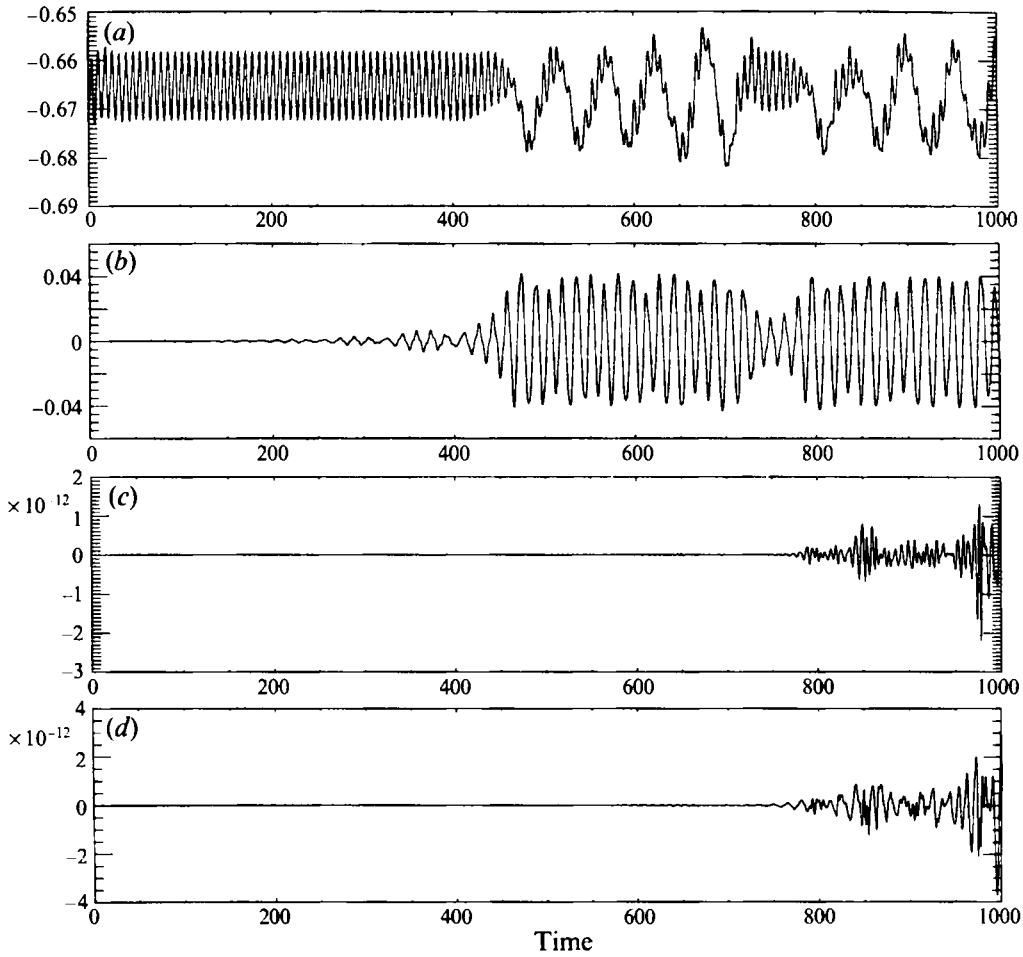

FIGURE 14. Time traces of lowest zonal-correction modes, $F = 1.53$, $Q = 0.10$: (*a*) symmetric baroclinic, (*b*) asymmetric barotropic, (*c*) symmetric barotropic, (*d*) asymmetric baroclinic.

time trace of the baroclinic wavy kinetic energy for $F = 1.25$, well below the critical value $F_c = 1.42$. The behaviour is similar to that exhibited by the same mode in figure 14, where the nonlinearities cause a low-frequency large-amplitude modulation, on which is superimposed a smaller, AV-type frequency.

For $Q = 0.15$ and 0.20 there exist stable AV regimes over a finite range of F. In both situations, the AV solution yields to a narrow range of quasi-periodic behaviour before becoming chaotic. Figure 15 displays time traces of the baroclinic wavy kinetic energy for $Q = 0.20$ and $F = 1.85$, 2.50, 3.75 and 4.20. These values of F correspond to steady, periodic, quasi-periodic, and chaotic behaviour, respectively. The levels of quasi-periodicity and chaos seen at $Q = 0.2$ are quite small and result only in a weak departure from amplitude vacillation. This should be contrasted with the chaotic behaviour found for $Q = 0.08$, where the amplitude deviations are much larger.

Figure 16(*a*) show the behaviour of the streamfunctions over one period in the periodic regime for $Q = 0.2$ and $F = 2.50$. The colour displays the barotropic portion, while the black contours show the baroclinic part. For both variables, the time-averaged mean has been removed in order to better show the spatio–temporal

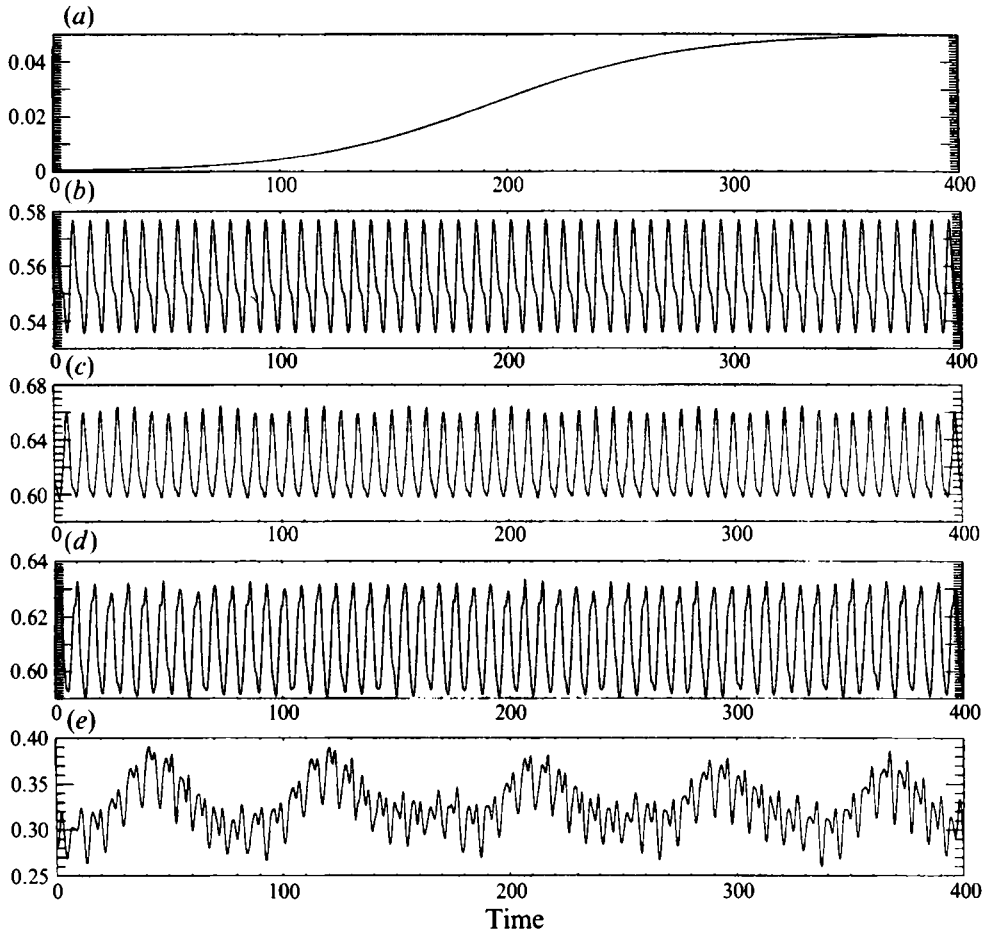

FIGURE 15. Time traces of baroclinic wavy kinetic energy in several regimes: (*a*) $F = 1.85$, $Q = 0.2$ (steady); (*b*) $F = 2.50$, $Q = 0.2$ (periodic); (*c*) $F = 3.75$, $Q = 0.2$ (quasi-periodic); (*d*) $F = 4.20$, $Q = 0.2$ (chaotic); (*e*) $F = 1.25$, $Q = 0.08$ (chaotic).

dynamics. The shift–reflect symmetry can clearly be seen. Although the system is periodic, the flow exhibits quite complicated spatial behaviour. In figure 16(*b*), the barotropic and baroclinic stream functions are displayed in a subcritical chaotic regime ($Q = 0.08$, $F = 1.25$) for six times with an interval equal to about 2 AV oscillation periods. The spatial fields again are complicated. The lack of shift–reflect symmetry is apparent since all modes are generally non-zero.

For $Q = 0.125$, the bifurcation sequence is slightly different. At $F = F_c = 1.60$, there is a transient AV regime that eventually becomes chaotic. However, at $F = 2.10$, there is an inverse bifurcation which causes the system to return to a symmetric, AV state. This behaviour continues until $F = 2.30$, at which point a symmetric zonotropic instability grows and results in quasi-periodic behaviour. The quasi-periodic solution is stable until $F = 2.40$, when both asymmetric modes grow and again cause chaos. These solutions bridge the gap between those seen at $Q = 0.10$ and those observed for $Q = 0.15$ or $Q = 0.20$.

One set of runs was carried out for F fixed at $F = 1.9$ with variable Q, the results of which are also displayed in figure 13(*a*). This was done in order to examine the

continuity of solutions in parameter space as Q was varied. At $Q = 0.2$, a symmetric steady solution is obtained. This persists until $Q \approx 0.16$, at which point a symmetric zonoclinic instability occurs, resulting in AV. If perturbed with a small-amplitude asymmetric nudge, the system returns to AV for $0.10 < Q < 0.16$, but becomes chaotic for $Q \leqslant 0.10$. However, a sufficiently large asymmetric perturbation results in a transition to chaos for $Q < 0.15$. This indicates that hysteresis is present for $Q < 0.15$.

7. Re-examination of the transitional region

Our original numerical results indicated that the transition from $\gamma < 0$ to $\gamma > 0$ behaviour occurs as Q crosses $Q_c = 0.15$, whereas the theory (figure 8) predicts that γ changes sign when $Q = Q_t \approx 0.13$. Upon further examination, the full numerical code revealed that very small-amplitude supercritical solutions do indeed exist for $Q \lesssim Q_c$, but that subcritical behaviour exists for larger amplitudes (hence the two steady solutions shown for $F \approx F_c$ and $Q = 0.15$ in figure 13*b*). This situation may occur if the A^3 term in (44) is stabilizing, but a higher-order A^5 term is destabilizing, requiring in turn a stabilizing A^7 term to bring the system to eventual equilibration. Although such a higher-order model is not directly obtainable by weakly nonlinear cascade, the structures of the bifurcation diagrams from such a heuristic system resemble those obtained numerically. For example, the various higher-order bifurcation diagrams are sketched in figure 17. Figure 17(*a*) illustrates the typical subcritical bifurcation diagram that exists for $Q \approx 0.10$. In figure 17(*b*), we see the situation when the A^3 term is stabilizing but the A^5 term is destabilizing. This is applicable for $Q \approx 0.15$. In this case, small initial conditions started at F slightly greater than F_c will evolve to the small supercritical branch near the origin. However, if the initial perturbation is too large, then the solution will jump up to the subcritical branch. This can be seen for $Q = 0.15$ in figure 13(*b*), where the system jumps from the supercritical steady solution (S_1) to the subcritical one (S_2) as F is decreased very slightly. Finally, for $Q \approx 0.20$ (figure 17*c*), the instability is purely supercritical, with no hysteresis or multiple solutions observed.

Although the existence of a subcritical bifurcation structure is predicted by the weakly nonlinear theory and confirmed by the numerical results, the structure itself is not easily obtainable directly from the numerical simulations, since the unstable solutions will never be realized. In order to extract such information, empirical orthogonal function (EOF) models were utilized. The methodology of constructing such models is discussed by Rodriguez & Sirovich (1990) and is explored in more detail in the context of two-layer channel flow with free-slip sidewalls by Mundt & Hart (1994). The crux of the method is to find basis functions which optimally describe the behaviour of the chosen system by appealing to data from the model itself. These models often prove useful because of their ability to accurately model relatively complex spatio–temporal behaviour with a small number of equations. In addition, EOF-based systems allow the determination of unstable steady states and, consequently, bifurcation structure.

EOF models were constructed at $Q = 0.10$, $F = 1.55$, and also at $Q = 0.2$, $F = 2.50$. These parameter settings were chosen in order to obtain one model representative of the subcritical region and one reflective of the supercritical regime. A model constructed in the mixed regime was not successful in replicating the pertinent bifurcation structure; the failure was due to numerical errors which prevented the resolution of the supercritical stable fixed point. For both sets of parameter settings used, the EOFs were obtained in an AV regime. Although for $Q = 0.10$ this behaviour is transient, the spatial fields were sampled well before the other instabilities reached

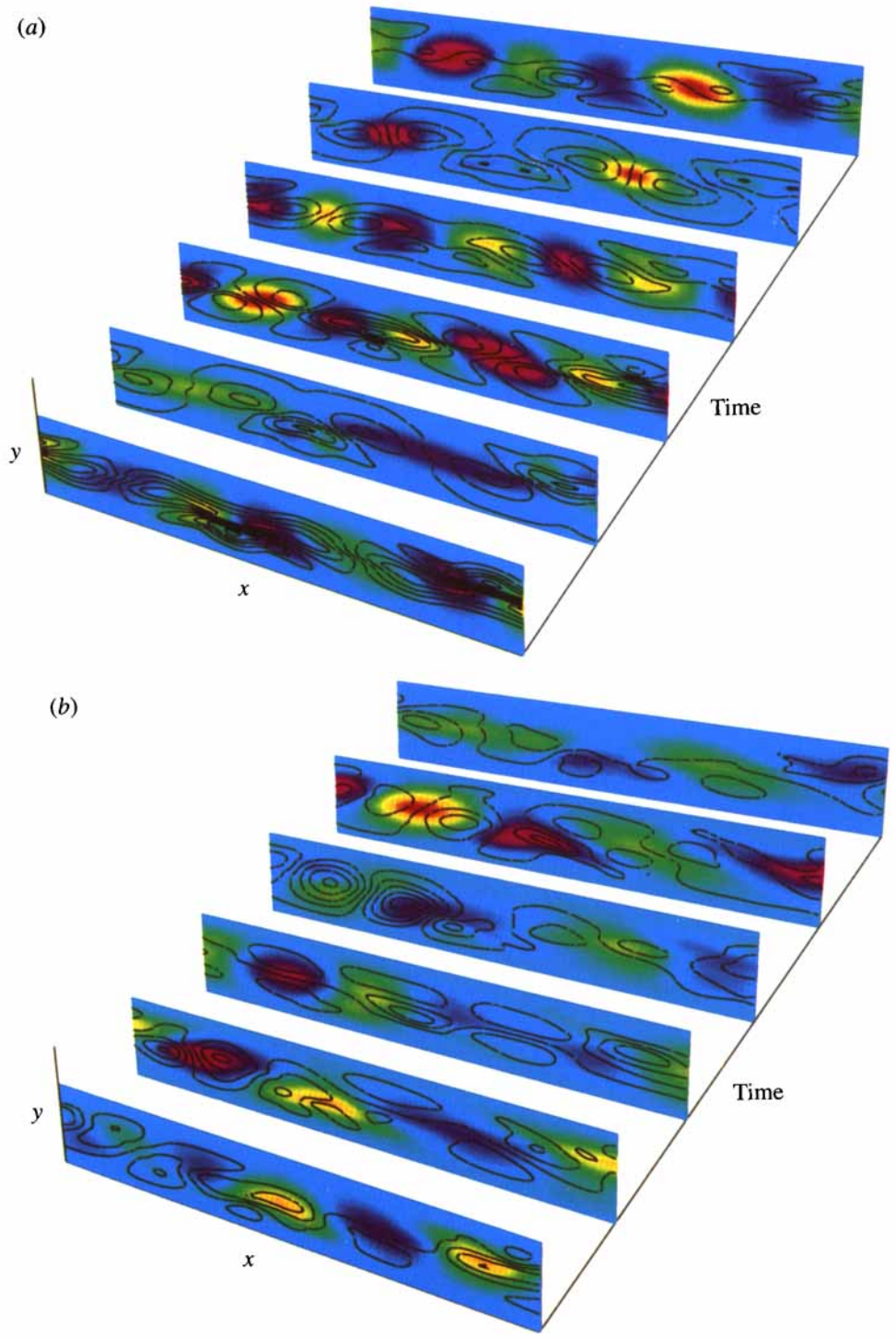

FIGURE 16. Barotropic (colour) and baroclinic (black contours) streamfunctions. (*a*) $Q = 0.20$, $F = 2.50$. The system is periodic, and the snapshots are taken every sixth of a period. (*b*) $Q = 0.08$, $F = 1.25$. The system is chaotic, and the snapshots are taken at time intervals of approximately two AV periods. In (*a*) and (*b*) the y-coordinate is stretched so that the flow near the sidewalls may be seen more clearly, and time increases from front to back.

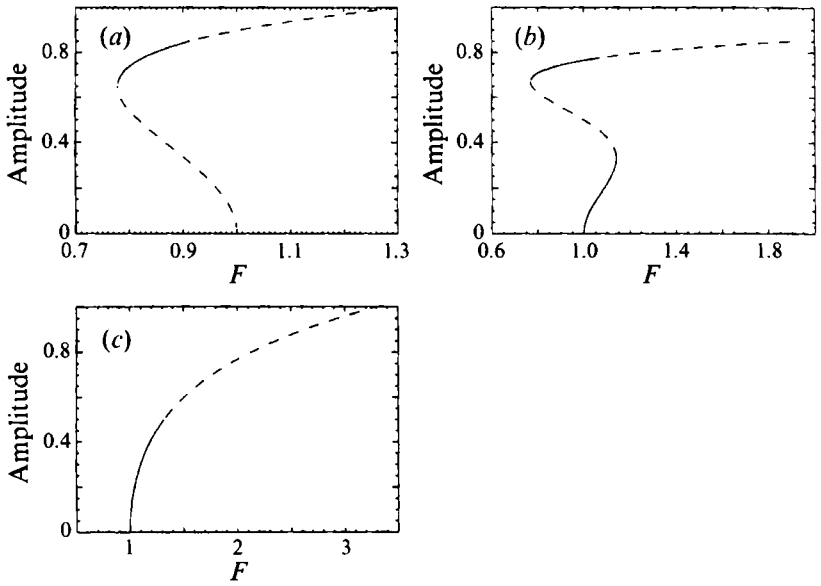

FIGURE 17. Various bifurcation structures seen in the rigid model: (*a*) $Q = 0.10$, purely subcritical bifurcation; (*b*) $Q = 0.15$, mixed bifurcation; (*c*) $Q = 0.20$, purely supercritical bifurcation. The solid and dashed lines indicate stable and unstable solutions, respectively. In all cases, $F_c = 1$, and the amplitudes are arbitrary.

a measurable amplitude. In both cases, four barotropic wavy EOFs, four baroclinic wavy EOFs, and three baroclinic zonal EOFs were necessary to model the flow accurately. The resulting sets of 11 ODEs were then used to find the fixed points of the system, and their stability, near F_c. The fixed points were found using Newton's root-finding method, and the stability of the fixed points was obtained by linearizing the governing equations about the steady state and examining the evolution of small perturbations. The only restriction is that the method implicitly assumes that the spatial behaviour remains constant throughout the chosen range of parameter space; the validity of this assumption was verified *a posteriori*. The results are shown in figure 18(*a*, *b*), where the amplitude of the baroclinic zonal correction is shown versus F.

At $Q = 0.1$, there is a clear subcritical bifurcation with an unsteady subcritical fixed-point branch emanating from near F_c (numerical errors prevented the resolution of the unstable fixed-point branch near the origin for $F > 1.36$), a small region in which there is a stable fixed point (near $F = 1.27$) and a supercritical fixed-point branch which is unstable to a Hopf bifurcation (the approximate amplitude of which is also shown). In contrast, for $Q = 0.2$, there is a supercritical stable fixed-point branch that begins at $F \approx 1.8$ and becomes unstable to a Hopf bifurcation at $F \approx 2.2$. The EOF models allow us to extract the numerical model's bifurcation structure and demonstrate that it is consistent with figure 17.

The presence of a mixed bifurcation diagram for $Q \approx 0.15$ can be inferred from the results of the full numerical simulations. Figure 19 displays the barotropic wavy kinetic energy versus F at $Q = 0.15$. The $\times$ symbols indicate the stable supercritical steady amplitudes, while the $+$ denote the stable subcritical steady values. The asterisks reflect the mean amplitudes of stable AV solutions. The bifurcation structure indicates that the supercritical steady solution persists for values of F only slightly greater than F_c (shown by the dashed line). Nonetheless, the shape is analogous to that shown in figure 17(*b*).

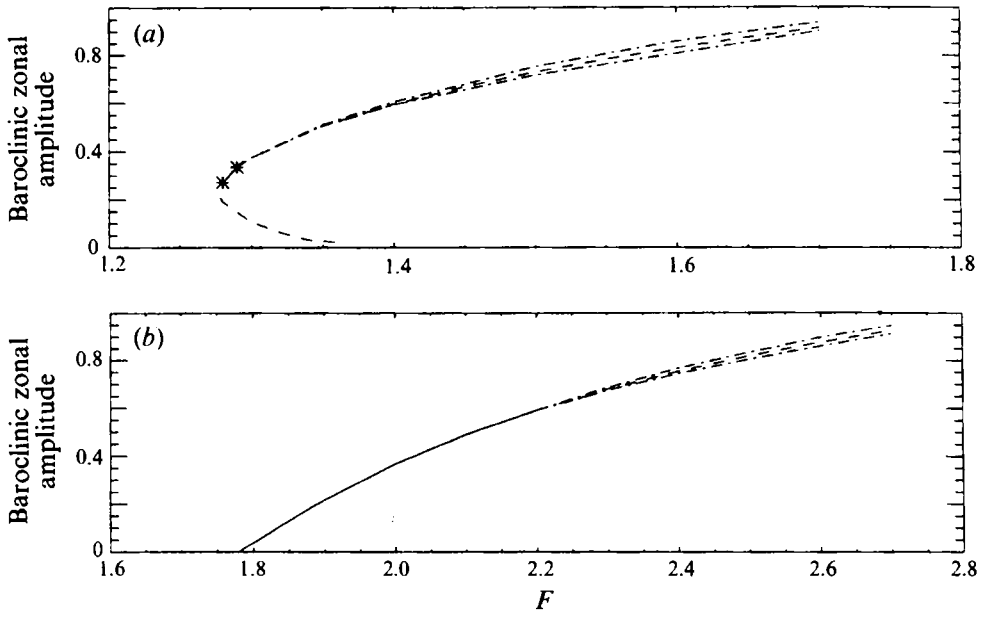

FIGURE 18. Bifurcation structure near $F_c = 1.52$ for (*a*) $Q = 0.1$, $E/R_0 = 0.001$ ($\Gamma = \sqrt{200}$); (*b*) $Q = 0.2$, $E/R_0 = 0.001$ ($\Gamma = \sqrt{400}$). The solid line shows a stable fixed point (in this case demarcated by asterisks), the dashed lines reflect unstable fixed points, and the dot-dashed lines show the approximate envelope of the stable periodic solution.

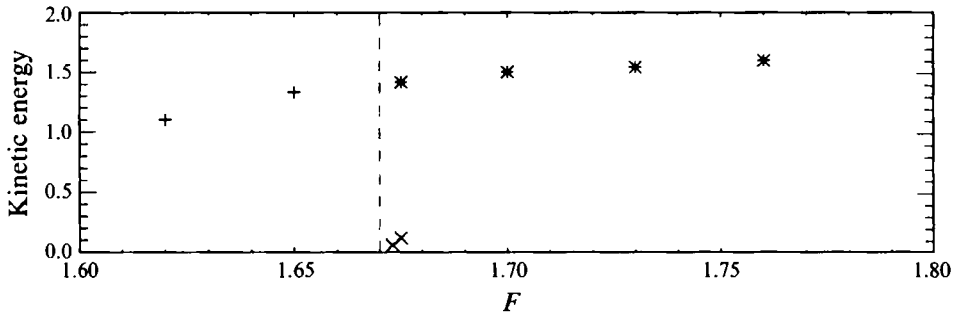

FIGURE 19. Mixed bifurcation structure as inferred from numerical simulations for $Q = 0.15$, $E/R_0 = 0.001$. The plot displays the barotropic wavy kinetic energy versus F. The × and + indicate stable, steady solutions, while the asterisks denote the mean amplitudes of periodic AV solutions. The dashed line denotes F_c.

8. Conclusions

The presence of rigid sidewalls has been shown to dramatically alter the behaviour of the baroclinic instability. For small enough bottom friction, the initial instability is subcritical, and chaotic behaviour can occur for negative supercriticality. Although the model geometry is different than that of typical laboratory experiments, the transition to chaos occurs, for the relevant parameter values, at approximately unit supercriticality. This compares well with previous *f*-plane experiments (Hart 1985), and it contrasts sharply with the transition to chaos at $F \approx 5F_c$ seen in previous numerical experiments performed with free-slip sidewalls. This indicates that the sidewall boundary layers are extremely important in determining the dynamical behaviour of baroclinic wave equilibration.

The application of the no-slip boundary condition leads to a sharp horizontal shear layer in the basic zonal current near each wall. These are fundamentally Stewartson layers in which lateral diffusion of vertical vorticity and stretching of planetary vorticity by Ekman suction exactly balance. For typical laboratory parameters the growing baroclinic waves feel the no-slip boundary condition through a narrower inner viscous boundary layer in which horizontal vorticity diffusion of the wave is balanced by advection in the strong basic-state vorticity gradients near the walls by normal velocities in the waves. The waves thus see an essentially inviscid horizontal basic shear outside this inner diffusion layer. The eigenfunctions of the basic baroclinic instability are somewhat altered in this shear layer. The effect on the perturbation streamfunctions does not appear large, compared with the stress-free case in which there is no basic horizontal shear. However, when we cascade these no-slip modes through to higher order, differentiations required to compute subsequent self-interaction vorticity advections magnifies these subtle influences and produces a substantially altered baroclinic zonal-flow vorticity gradient. The interaction between the basic barotropic wave and this second-order mean baroclinic vorticity gradient, especially in the Stewartson shear zones, leads to an enhancement of the linear growth rate, and for small enough bottom friction, to subcritical instability. In regions of subcritical instability, high-resolution numerical computations show that the baroclinic wave amplitudes can become very large, system symmetries are destroyed by secondary instability, and baroclinic chaos may be found at negative supercriticality.

It is natural to ask about effects of cylindrical geometry and ageostrophy on these processes. The cylinder is somewhat different in that there is only one wall, and this, coupled with the mechanism for driving the laboratory flows from the top only, eliminates both the flip–reverse and shift–reflect symmetries of our channel model. This should render the bifurcations observed in the present computations imperfect, and efforts to construct a multi-grid code to examine this are currently under way. Our simulations have shown that no-slip sidewalls dramatically reduce the supercriticality needed for chaos. However, one aspect of the laboratory experiments cannot be captured by this f-plane model. That is the observation (Hart 1985) that cyclonic forcing (anticyclonic outer wall layer) is significantly more unstable than anticyclonic driving (with a cyclonic Stewartson layer at the cylinder wall). One hypothesis under investigation is that this is due to nonlinear Ekman suction effects in the strong-vorticity zone at the sidewall that cause significant differences in shear profiles for the two driving methods.

This research was supported by the National Science Foundation under grant ATM-9025087. Computational resources were provided in part by NASA grant NAG8-190 and contract NAS8-31958. We are most grateful to these sponsors and to Drs Keith Julien and Fausto Cattaneo for helpful discussions.

REFERENCES

CANUTO, C., HUSSAINI, M. Y., QUARTERONI, A. & ZANG, T. A. 1988 *Spectral Methods in Fluid Dynamics*. Springer.

CATTANEO, F. & HART, J. E. 1990 Multiple states for quasi-geostrophic channel flows. *Geophys. Astrophys. Fluid Dyn.* **54**, 1–33.

HART, J. E. 1972 A laboratory study of baroclinic instability. *Geophys. Fluid Dyn.* **3**, 181–209.

HART, J. E. 1985 A laboratory study of baroclinic chaos on the f-plane. *Tellus* **37A**, 286–296.

HART, J. E. 1986 A model for the transition to baroclinic chaos. *Physica* D **20**, 350–362.

KLEIN, P. & PEDLOSKY, J. 1986 A numerical study of baroclinic instability at large super-criticality. *J. Atmos. Sci.* **43**, 1243–1262.

KLEISER, L. & SCHUMANN, U. 1980 In *Proc. 3rd Gesellschaft für Angewandte Mathematik and Mechanik Conf: Numerical Methods in Fluid Mechanics* (ed. E. H. Hirschel), p. 165. Vieweg.

MUNDT, M. & HART, J. E. 1994 Secondary instability, EOFs, and the transition to chaos in two-layer baroclinic instability with free-slip sidewalls. *Physica* D **78**, 65–92.

PEDLOSKY, J. 1970 Finite-amplitude baroclinic waves. *J. Atmos. Sci.* **27**, 15–30.

PEDLOSKY, J. 1971 Finite-amplitude baroclinic waves with small dissipation. *J. Atmos. Sci.* **28**, 587–597.

PEDLOSKY, J. 1972 Limit cycles and unstable baroclinic waves. *J. Atmos. Sci.* **29**, 53–63.

PEDLOSKY, J. 1987 *Geophysical Fluid Dynamics*, 2nd Edn. Springer.

PEDLOSKY, J. & FRENZEN, C. 1980 Chaotic and periodic behavior of finite-amplitude baroclinic waves. *J. Atmos. Sci.* **37**, 1177–1196.

PEDLOSKY, J. & KLEIN, P. 1991 The nonlinear dynamics of slightly supercritical baroclinic jets. *J. Atmos. Sci.* **48**, 1276–1286.

PHILLIPS, N. A. 1954 Energy transformations and meridional circulations associated with simple baroclinic waves in a two-level, quasi-geostrophic model. *Tellus* **6**, 273–286.

RODRIGUEZ, J. D. & SIROVICH, L. 1990 Low-dimensional dynamics for the Ginzburg–Landau equation. *Physica* D **43**, 77–86.

STEWARTSON, K. 1957 On almost rigid rotations. *J. Fluid Mech.* **3**, 17–26.